Solar Phys (2020) 295:126
https://doi.org/10.1007/s11207-020-01694-0

EDITORS' CHOICE

Analysis of Large Deflections of Prominence–CME Events during the Rising Phase of Solar Cycle 24

M. Valeria Sieyra[1] · **Mariana Cécere**[2] · **Hebe Cremades**[1] · **Francisco A. Iglesias**[1] · **Abril Sahade**[2] · **Marilena Mierla**[3,4] · **Guillermo Stenborg**[5] · **Andrea Costa**[2] · **Matthew J. West**[3] · **Elke D'Huys**[3]

Received: 11 April 2020 / Accepted: 18 August 2020 / Published online: 9 September 2020

Abstract The analysis of the deflection of coronal mass ejection (CME) events plays an important role in the improvement of the forecasting of their geo-effectiveness. Motivated by the scarcity of comprehensive studies of CME events with a focus on the governing conditions that drive deflections during their early stages, we performed an extensive analysis of 13 CME events that exhibited large deflections during their early development in the low corona. The study was carried out by exploiting solar-corona-imaging observations at different heights and wavelengths from instruments onboard several space- and ground-based solar observatories, namely the *Project for Onboard Autonomy 2* (PROBA2), *Solar Dynamics Observatory* (SDO), *Solar TErrestrial RElations Observatory* (STEREO), *Solar and Heliospheric Observatory* (SOHO) spacecraft, and from the National Solar Observatory (NSO). The selected events were observed between October 2010 and September 2011, to take advantage of the location in near quadrature of the STEREO spacecraft and Earth in this time period. In particular, we determined the 3D trajectory of the front envelope of the CMEs and their associated prominences with respect to their solar sources by means of a forward-modeling and tie-pointing tool, respectively. By using a potential-field source-

---

This article belongs to the Topical Collection:
PROBA-2 at Ten Years
Guest Editors: Elke D'Huys, Marie Dominique and Matthew J. West

---

✉ M.V. Sieyra
valeria.sieyra@frm.utn.edu.ar

M. Cécere
mariana.cecere@unc.edu.ar

H. Cremades
hebe.cremades@frm.utn.edu.ar

[1] Universidad Tecnológica Nacional – Facultad Regional Mendoza, CONICET, CEDS, Rodriguez 243, Mendoza, Argentina

[2] Instituto de Astronomía Teórica y Experimental, CONICET-UNC, Córdoba, Argentina

[3] Solar-Terrestrial Center of Excellence—SIDC, Royal Observatory of Belgium, Brussels, Belgium

[4] Institute of Geodynamics of the Romanian Academy, Bucharest, Romania

[5] Space Science Division, US Naval Research Laboratory, Washington, DC 20375, USA

surface model, we estimated the coronal magnetic fields of the ambient medium through which the events propagate to investigate the role of the magnetic-energy distribution in the non-radial propagation of both structures (front envelope and prominence) and in their kinematic properties. The ambient magnetic environment during the eruption and early stages of the events is found to be crucial in determining the trajectory of the CME events, in agreement with previous reports.

Keywords Coronal Mass Ejections, Low Coronal Signatures · Coronal Mass Ejections, Initiation and Propagation · Magnetic fields, Corona · Prominences, Quiescent · Prominences, Active

1. Introduction

Coronal mass ejections (CMEs) are large-scale phenomena that constantly erupt from the solar surface traveling through interplanetary space. They constitute one of the primary drivers of space-weather events, such as geomagnetic storms, solar energetic particles, etc. When assessing the capacity of a particular CME to affect Earth or another natural or artificial object, it is, of course, important to have knowledge of its magnetic-field orientation and other energy-related parameters. However, in the first place, it is of utmost importance to correctly ascertain its propagation direction and size, so as to determine whether the impact will take place at all, and this knowledge will also enable us to perform more accurate space-weather predictions.

It is well known that CMEs do not always propagate radially outward from their source regions (e.g. MacQueen, Hundhausen, and Conover, 1986; Gosling et al., 1987; Vandas et al., 1996; Cremades and Bothmer, 2004; Gui et al., 2011; Rollett et al., 2014; Kay, Opher, and Evans, 2015; Möstl et al., 2015) and determining their direction of propagation may not be straightforward from a single viewpoint, particularly if the CME is directed towards it. Since the launch of the *Solar TErrestrial RElations Observatory* (STEREO: Kaiser et al., 2008) together with the development of various reconstruction tools (e.g. Mierla et al., 2008, 2010; Maloney, Gallagher, and McAteer, 2009; de Koning, Pizzo, and Biesecker, 2009; Temmer, Preiss, and Veronig, 2009; Srivastava et al., 2009; Liewer et al., 2009; Thernisien, Vourlidas, and Howard, 2009, 2011; Liu et al., 2010), it is possible to obtain three-dimensional (3D) information of CMEs and their associated prominences. This allows us to determine the deflection in latitude as well as in longitude from the source location for both structures. It has also provided new insights into the relationship between various features associated with filaments and CME eruptions.

Moreover, to date it has not been possible to predict before eruption whether a specific CME, to be born in a particular region on the Sun under specific environmental conditions, is to be deflected and to what extent. Although there are some studies in this direction (e.g. Kay, Opher, and Evans, 2015; Zhuang et al., 2017) the detailed analysis on the causes of deflection are focused only on case studies (e.g. Gui et al., 2011; Panasenco et al., 2013; Liewer et al., 2015; Kay et al., 2017; Cécere et al., 2020).

It has been shown that in activity-minimum years there is a systematic deflection to lower latitudes, but there is no systematic trend at times of high activity (e.g. Cremades and Bothmer, 2004; Wang et al., 2011). During solar minimum, the heliospheric current sheet (HCS) remains flat at low latitudes, so predominantly latitudinal deflections occur towards the Equator. During other times of the solar cycle, the HCS transitions to a more complex configuration, which would allow deflections to have a more significant longitudinal component, as suggested by Kay, Opher, and Evans (2015).

It is also widely known that CMEs propagate non-radially away from nearby coronal holes and toward regions of low magnetic energy. For example Cremades, Bothmer, and Tripathi (2006) found a good correspondence between the deflection of CMEs and the total area of coronal holes (CHs), suggesting that the neighboring CHs affect the evolution of CMEs near the Sun. Gopalswamy et al. (2009) also suggested that CMEs could be deflected by the associated CHs and claimed that the open flux from these structures acted as magnetic walls, constraining CME propagation. The work performed by Shen et al. (2011) showed that the trajectories of the analyzed CMEs were influenced by the background magnetic field, and that they are likely to deflect to the nearby region with lower magnetic-energy density. Gui et al. (2011), extending the work of Shen et al. (2011) to ten CMEs, analyzed the deflection in both latitude and longitude. Aside from verifying the previous results, they found a positive correlation between the deflection rate and the strength of the gradient of the magnetic-energy density.

In addition to these causes, recent studies have demonstrated that CMEs are also deflected by strong magnetic fields from active regions in the locations of the CME source (e.g. Möstl et al., 2015; Wang et al., 2015; Kay, Opher, and Evans, 2015; Kay et al., 2017), with the magnitude of the deflection being inversely related to CME speed and mass. This was previously suggested by Xie et al. (2009) and Kilpua et al. (2009). Slower and wider CMEs deflect toward the Equator during solar minimum while faster and narrower CMEs deflect less; in some cases they even propagate radially from their source active region. It was suggested that slow and wider CMEs cannot penetrate through the background overlying coronal fields, but they are channeled toward the streamer belt. Also the background fast solar wind can inhibit the latitudinal expansion of the CME in the corona (e.g. Cremades, Bothmer, and Tripathi, 2006) and interact with CMEs at large distances (e.g. Isavnin, Vourlidas, and Kilpua, 2014) where the magnetic forces from the background are negligible. Recent numerical research by Zhuang et al. (2019) supports CME deflection in interplanetary space relative to the difference between CME and solar-wind speed, i.e. the greater the difference, the larger the deflection. Interactions between multiple CMEs/ICMEs can also cause deflections, mainly longitudinal (e.g. Lugaz et al., 2012; Shen et al., 2012; Liu et al., 2012, 2014). In summary, the rate and amount of CME deflection are believed to be controlled by the strength and distribution of the background magnetic field, and the mass, size, and speed of the CME relative to the solar wind. Hence, both the global and the local configuration of the Sun's magnetic field together with intrinsic CME properties would have crucial importance for the degree and direction of deflection.

At the same time, prominence deflection and rolling motions during the process of eruption have received less attention, although there has been some work along these lines (e.g. Filippov, Gopalswamy, and Lozhechkin, 2001; Martin, 2003; Panasenco and Martin, 2008; Bemporad, 2009; Panasenco et al., 2011; Pevtsov, Panasenco, and Martin, 2012; Liewer, Panasenco, and Hall, 2013). The filament, the channel encompassing the polarity reversal boundary, the overlying arcade, and the CME itself are all part of one linked magnetic system (Martin et al., 2008; Pevtsov, Panasenco, and Martin, 2012). The filament eruption and the CME are two manifestations of the same underlying magnetic phenomenon; thus by studying filament eruptions we can better understand CME triggering and improve our ability to predict it. Very few studies combine the dynamics of the prominence and CME. For example Panasenco et al. (2013) demonstrated that major twists and non-radial motions in erupting filaments and CMEs are typically related to the larger-scale ambient conditions around the eruptive events. They found that the non-radial propagation of both structures is correlated with the presence of nearby coronal holes and is guided towards weaker field regions, namely null points existing at different heights in the overlying magnetic configuration. The CME propagates in the direction of least resistance, which is always away from the coronal hole, and the non-radial direction of the erupting filament system is caused either by the open coronal-hole magnetic field near the filament channel or by other strong magnetic field, which might be in the neighborhood of the eruption. They also found that the non-radial motion of the prominence is greater than that of the CME. Another study that considers the magnetic background surrounding the source region is reported by Liewer et al. (2015). They analyzed the coronal magnetic pressure forces acting on CMEs at different heights in the corona and also consider the non-radial propagation below the coronagraph field of view (FOV). They concluded that non-radial propagation can result not only from large-scale coronal fields, but also from initial asymmetric expansion caused by the nearby strong active-region fields. They found that CMEs propagate through the weak-field region around the HCS and do not follow the shortest path to the HCS, but the path depends on the local and global gradients in the magnetic pressure.

Given the importance of understanding non-radial propagation to improve our ability to forecast whether or not a CME will impact Earth, and motivated by the lack of statistical studies that analyze the whole erupting system focusing on the main causes of deflection, we perform a systematic study of the deflection of CMEs and their associated prominences with respect to their solar sources. Taking advantage of the spacecraft fleet dedicated to studying solar activity including the *Solar and Heliospheric Observatory* (SOHO: Domingo, Fleck, and Poland, 1995), the *Solar Dynamics Observatory* (SDO: Pesnell, Thompson, and Chamberlin, 2012), the *Project for Onboard Autonomy 2* (PROBA2: Santandrea et al., 2013), the *Solar-Terrestrial Relations Observatory* (STEREO: Kaiser et al., 2008), and the National Solar Observatory (NSO) together with the reconstruction methods mentioned above, we determine the trajectory of CMEs and their corresponding prominences. Considering the coronal magnetic fields as computed from a potential field source surface model (PFSS: Schrijver and De Rosa, 2003) we attempt to investigate the roles of magnetic-energy distribution and kinematic features in the non-radial propagation of both structures.

The methodology, including the identification criteria used to compile the analyzed events, the methods to determine the trajectory of the prominences and CMEs, and the estimation of the magnetic energy at different heights, is described in Section 2. The results obtained, both in relation to the kinematics and the magnetic environmental conditions are presented in Section 3 together with a detailed analysis of some specific cases in Section 3.3. Finally, we discuss and summarize our main findings in Section 4.

2. Observations and Methodology

2.1. Data and Events Selection

Since our main interest entails the investigation of CME events having large deflections with respect to their solar sources, we pre-select candidate events for the study by means of the following procedure: first, we considered all filament eruptions reported by the *AIA Filament Eruption Catalog* (McCauley et al., 2015) from October 2010 until September 2011. We chose this time interval because the quadrature location between spacecraft on the Sun–Earth line and the STEREO twin probes provides a better three-dimensional perspective of the prominences and associated CMEs. Out of the 183 filament eruptions reported by the *AIA Filament Eruption Catalog* during that time interval,

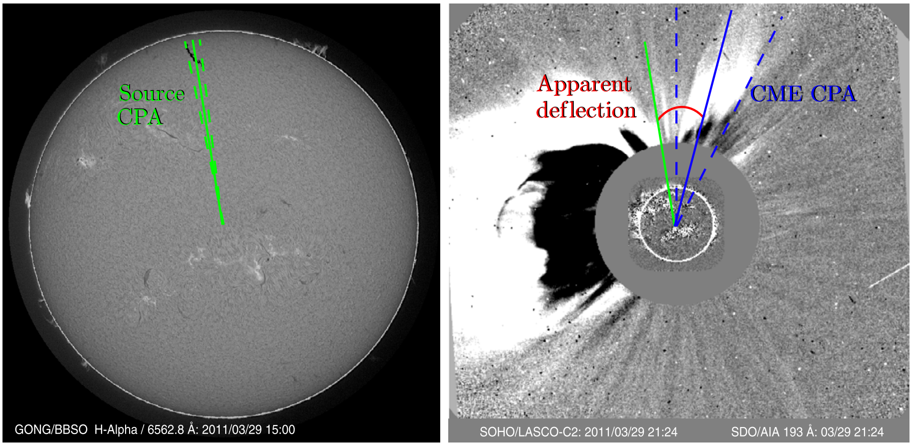

Figure 1 Apparent deflection from Earth's view defined by the difference in position angle between the middle point of the source region (Source CPA, left panel) and the central position angle of the CME (CME CPA, right panel). The source is seen in Hα image from BBSO at 15:00 UT and the CME image is taken from SOHO/LASCO-C2 at 21:24 UT on 29 March 2011.

we found 118 events that resulted in CMEs detected in the field of view of white-light coronagraphs. The erupting filament–CME associations were performed with the aid of the SOHO/LASCO CME Catalog (Yashiro et al., 2004). Next, to pre-select candidate events having large deflections, we checked for large differences ($\gtrsim 20^\circ$) between position angles of the filaments before erupting and of their ensuing CMEs, both angles measured on the plane of sky from the same viewpoint and counterclockwise from the solar north. We chose a value of 20° in agreement with the average unsigned deflection found by Cremades, Bothmer, and Tripathi (2006).

To measure the position angle of the central point of the filament (Source CPA) in its pre-eruptive phase we used images in Hα from the *Global Oscillation Network Group* (GONG: Kennedy and GONG Team, 1994) from the *National Solar Observatory Integrated Synoptic Program* (NISP). Whenever the source pre-eruptive filament could not be fully detected in Hα, either because it was too faint in this wavelength or its location was not on the visible side as seen from Earth, we used images from extreme-ultraviolet (EUV) telescopes, namely the *Atmospheric Imaging Assembly* (AIA: Lemen et al., 2012) onboard SDO and the *Sun–Earth Connection Coronal and Heliospheric Investigation EUV Imager* (SECCHI-EUVI: Howard et al., 2008) onboard the twin STEREO spacecraft. CME central position angles (CPA) were measured on images from LASCO-C2 (*Large Angle and Spectrometric Coronagraph Experiment*: Brueckner et al., 1995) and SECCHI-COR2 at a height of $\approx 5\ R_\odot$ (projected on the plane of sky), assuming that CMEs are fully developed and their evolution is self-similar at this height. A scheme that clarifies the pre-selection criterion is presented in Figure 1. The left panel of the figure displays an Hα image from Big Bear Solar Observatory (BBSO), where the dashed-green lines encompass the filament that erupts later, and the solid-green line indicates the Source CPA considered as the source of the CME. The right panel shows the associated CME as seen by SOHO/LASCO-C2, with the dashed-blue lines encompassing the CME's angular width and the solid line its CME CPA. The difference between these CPAs, shown in red, represents the deflection projected onto the plane of sky of the instrument (apparent deflection). It is worth noting that the explosive CME on the east limb does not affect the trajectory of the event under study, close to the North Pole. It is evident from the SDO/EUVI observations that the latter had already been deflected, before the shock wave of the east limb CME reaches it.

After this pre-selection of events whose projected deflection on the basis of CPAs is greater than 20°, we further constrain our sample by examining whether that apparent, i.e. projected, deflection corresponds to a real deflection. The overall "real" (i.e. 3D) deflection is defined by the difference in latitude [$\Delta\Theta$] and Carrington longitude [$\Delta\Phi$] between the central coordinates of the source region, i.e. those of the filament in its pre-eruptive state, and the coordinates of the resulting CME at the greatest measured height. The methods used to deduce the 3D coordinates (latitude, longitude, and height) of CMEs and source regions, among another parameters, are described in Section 2.2.

On the basis of spherical trigonometry, the 3D deflection is defined as

$$\Psi_i(h) = \arccos(\sin(\Theta_{\mathrm{src}})\sin(\Theta_i(h)) + \cos(\Theta_{\mathrm{src}})\cos(\Theta_i(h))\cos(\Phi_{\mathrm{src}} - \Phi_i(h))) \qquad (1)$$

where $0 < \Psi(h) < \pi$, Θ_{src} and Φ_{src} are the latitude and longitude associated with the source region, respectively, $\Theta_i(h)$ and $\Phi_i(h)$ are the latitude and longitude at different heights. The index i denotes either the prominence or the CME. Thus, we define the total 3D deflection as $\Delta\Psi = \Psi_{\mathrm{cme}}(h = h_f)$, where h_f is the final CME measured height. A given event is selected for further analysis only if $\Delta\Psi \gtrsim 20°$. Out of the 118 events reported by the *AIA Filament Eruption Catalog* during the investigated time interval, 23 were initially pre-selected as they exhibited a projected deflection $|\Delta\mathrm{CPA}| \gtrsim 20°$; but only 13 of these events yielded total 3D deflections $\Delta\Psi \gtrsim 20°$ according to our measurement method. The 10 remaining events were discarded due to several reasons: either their total 3D deflections were small ($\Delta\Psi < 20°$), or there were data gaps in COR2 or LASCO, or the CMEs were too faint to deduce their latitude and longitude applying the method described in the following section. The 13 selected events that satisfy $\Delta\Psi \gtrsim 20°$ are summarized in Table 1. The table indicates CPAs and coordinates (latitude Θ and longitude Φ) of the source region and CME, the difference between these measurements and the obtained total 3D deflection. We also show the distribution of the resulting deflection in latitude, longitude and 3D for the selected events in Figure 2. Most of the events present latitudinal deflection between 10° and 20° and a longitudinal deflection lower than 10°, while there are fewer events that exhibit deflections larger than 50° in both coordinates. The total 3D deflection $\Delta\Psi$ reaches values between 20° and 30°. This figure also indicates that our sample of events presents latitudinal and longitudinal deflections in similar ranges.

2.2. Determination of 3D Coordinates and Tracking

2.2.1. Coordinates

After the pre-selection procedure, we determined 3D coordinates of the source region and ensuing CME, to ascertain whether the apparent deflection was indeed related to a real deflection similar to or larger than 20°. To determine the 3D coordinates of the source region, which we defined as the central position coordinates of the filaments in their pre-eruptive state, we used Hα images from the NSO/GONG Hα Archive using standard SolarSoft procedures. In those cases where the filament was not clearly discernible in that wavelength, or it was too close to the limb, or on the farside, we measured the coordinates in SDO/AIA or STEREO/EUVI 304 Å images by means of the JHelioviewer (Müller et al., 2017) image visualization tool.

Table 1 The 13 selected events that satisfy $|\Delta\mathrm{CPA}| \gtrsim 20^\circ$ and $\Delta\Psi \gtrsim 20^\circ$ between October 2010 and September 2011. The first two columns display the *AIA Filament Eruption Catalog* ID and the date of the reported event, columns 3 – 5 indicate the source region location (CPA, latitude and Carrington longitude), columns 6 – 9 exhibit the CME first appearance time in LASCO-C2 and location parameters, while columns 10 – 13 show the resulting deflection in position angle, latitude, and longitude, as well as the total 3D deflection.

Catalog		SR			CME				Deflection			
ID	Date	CPA	Θ	Φ	Time*	CPA	Θ	Φ	ΔCPA	$\Delta\Theta$	$\Delta\Phi$	$\Delta\Psi$
(1)	(2)	(3)	(4)	(5)	(6)	(7)	(8)	(9)	(10)	(11)	(12)	(13)
118	24 Nov 2010	344^{b}	62	76	07:36	325	43	67	−19	−19	−9	20
132	16 Dec 2010	298^{d}	29	110	08:48	326	43	138	28	14	28	26
136	23 Dec 2010	212^{a}	−53	66	05:00	234	−17	33	22	36	−33	44
142	02 Jan 2011	209^{b}	−58	347	06:12	255	−5	347	46	53	0	53
159	30 Jan 2011	320^{a}	25	250	18:36	278	7	272	−42	−18	22	28
180	25 Feb 2011	34^{a}	43	208	08:00	348	45	263	46	2	55	39
196	27 Mar 2011	354^{a}	68	205	20:12	324	51	255	−30	−17	50	29
197	29 Mar 2011	9^{a}	51	169	20:36	347	64	224	22	13	55	31
216	13 May 2011	216^{a}	−38	357	18:48	254	−8	351	38	30	−6	30
251	07 Jul 2011	119^{a}	−19	252	13:25	99	1	244	−20	20	−8	21
274	10 Aug 2011	310^{c}	41	43	05:00	334	64	49	24	23	6	23
276	11 Aug 2011	287^{b}	18	291	10:36	267	−1	269	20	−19	−22	29
286	08 Sep 2011	60^{c}	28	226	06:12	38	47	240	−22	19	14	22

* First LASCO-C2 appearance time [UT].

[a] Measured using Hα images.

[b] Measured using SDO/AIA images.

[c] Measured using STEREO-A/EUVI.

[d] Measured using STEREO-B/EUVI.

As central 3D coordinates of each CME, we considered those yielded by the Graduated Cylindrical Shell (GCS) forward model (Thernisien, Howard, and Vourlidas, 2006; Thernisien, Vourlidas, and Howard, 2009) at the highest possible altitude, dependent on the particular visibility conditions of each case. This method reproduces the large-scale structure of a flux-rope-like CME by modeling its outer envelope as a hollow croissant-like shape. Briefly, the model consists of a tubular section forming the main body of the structure attached to two cones that correspond to the “legs” of the CME. Fitting the GCS model to the CMEs in the SOHO/LASCO and STEREO/COR2 coronagraph images enables us not only to estimate their 3D direction of propagation (longitude and latitude), but also their apex height, half angular width, tilt angle of the symmetry axis with respect to the solar Equator, and aspect ratio. The quadrature position of the STEREO spacecraft with respect to those on the Sun–Earth line is advantageous to minimize uncertainties in the determination of the GCS parameters (e.g. Cremades, Iglesias, and Merenda, 2020).

As anticipated in Section 2.1, the 3D latitude and longitude determined for the source regions and CMEs (columns 4, 5, 8, and 9 from Table 1) are used to calculate deflection in the latitudinal and longitudinal directions (columns 11 and 12), as well as the total 3D deflection (last column of Table 1). The kinematic and magnetic analysis is applied only to those events exhibiting a total 3D deflection $\Delta\Psi \gtrsim 20^\circ$.

Figure 2 Distribution of the deflection in latitude (upper panel), longitude (central panel), and 3D (bottom panel) for the analyzed events. The deflections shown here were calculated considering the central coordinates of the source region and the coordinates of the associated CME apex at its highest measured point.

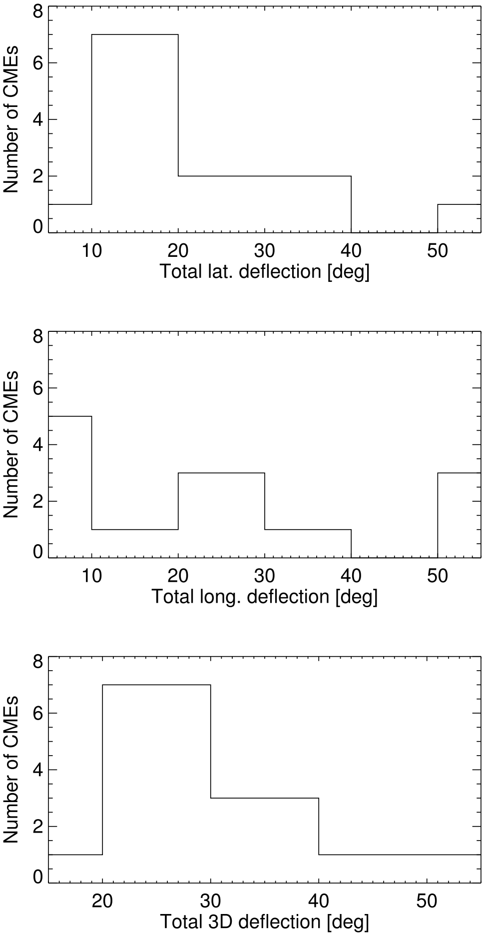

2.2.2. *Tracking*

Although Table 1 lists the total deflection for each event, we are mostly interested in analyzing the spatio–temporal evolution of these deflections. We achieve this by tracking in time the 3D location of the erupting prominences and associated CMEs. To characterize the evolution of the prominence material we use the tie-pointing/triangulation reconstruction technique, (see, e.g., Inhester, 2006; Mierla et al., 2008, 2009) on EUV images from SDO/AIA, STEREO/EUVI, and *Sun Watcher using Active Pixel System detector and Image Processing* (SWAP: Seaton et al., 2013; Halain et al., 2013) onboard PROBA2. The method uses a pair of images to trace the line-of-sight of a specific point selected in one image into the FOV of the second image. This line is called the epipolar line (see Inhester, 2006, for details on the epipolar geometry). The tie-pointing method is convenient when the triangulated structure is compact and well defined, as is the case of prominences. In particular, we attempt to apply this method to parcels of prominence material in the EUV low corona, which can later be tracked to a feature in the CME's core as detected in coronagraph images.

In the top and middle panel of Figure 3 we show, for illustration purposes, two snapshots of the triangulation procedure for one of the events (29 March 2011) using SDO/AIA and

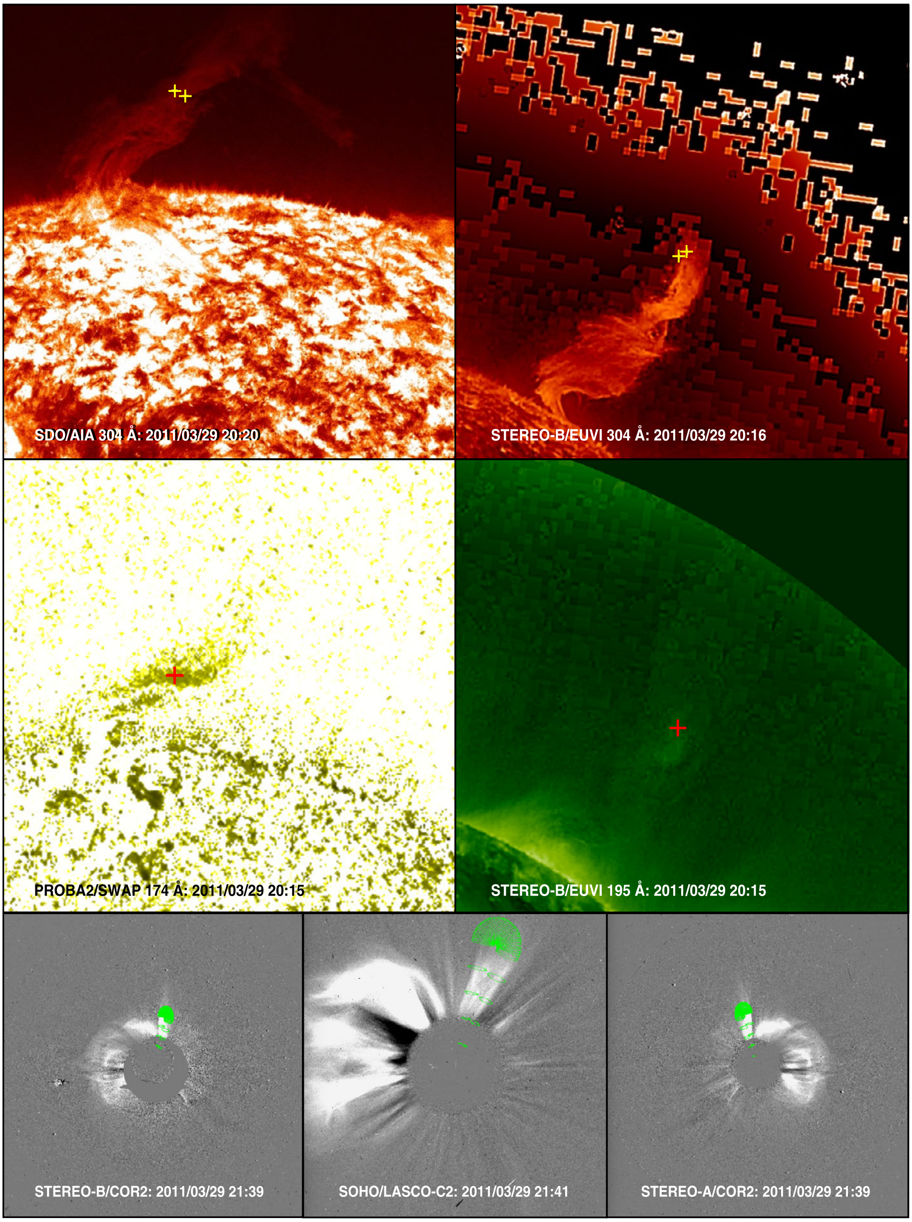

Figure 3 Top and middle panel: Triangulation of a parcel of the erupting prominence for the event of 29 March 2011. The top-left image corresponds to SDO/AIA 304 Å at 20:20 UT and the top-right to a wavelet-enhanced image of STEREO-B/EUVI 304 Å at 20:16 UT. In the middle panel, the left image is a processed image of PROBA2/SWAP 174 Å and the right one a wavelet-enhanced STEREO-B/EUVI 195 Å, both at 20:15 UT. Yellow (top) and red (middle) crosses indicate the parcel that is being triangulated to determine its 3D coordinates. Bottom panel: GCS model (green mesh) applied to the CME associated to the event on 29 March 2011. The left image corresponds to STEREO-B/COR2 at 21:39 UT, the central to SOHO/LASCO-C2 at 21:41 UT and the right one to STEREO-A/COR2 at 21:39 UT.

STEREO-B/EUVI, both in 304 Å (top), and PROBA2/SWAP 174 Å and STEREO-B/EUVI 195 Å (middle). The yellow crosses in each image indicate the parcel of filament that is triangulated to obtain its 3D coordinates. The parcel is triangulated until it either leaves the FOV of the EUV instruments or it becomes so faint that it cannot be further distinguished as a defined structure. For four events the prominence was clearly seen in the larger FOV of PROBA2/SWAP 174 Å; thus we triangulated the filament using this instrument together with 195 Å images from STEREO/EUVI (for example the event shown in Figure 3). We use EUVI 195 Å images instead of EUVI 171 Å because in general the cadence of 171 Å observations is very low (typically one image every two hours) compared to 195 Å, so the matching of these images with SWAP 174 Å is not possible most of the time. Therefore, to perform measurements in a systematic way, we chose 195 Å to accomplish this task. Although the prominence may appear different in the two wavelengths, the parcel of the prominence that is triangulated is usually located at the top of the structure and is easily recognizable as a bright feature against the dark background of the off-limb corona as the eruption progresses. For other studies using pairs of images in different wavelengths for the triangulation procedure please see Seaton et al. (2011) and Mierla et al. (2013). For those other events where the prominence was not discernible in the PROBA2/SWAP FOV, we used SDO/AIA 304 Å and STEREO/EUVI 304 Å for the triangulation. We also applied this technique to pairs of white-light images, whenever we can visually track the triangulated prominence parcel to the CME core seen by the coronagraphs.

To track the CME evolution, we implemented the GCS model at different instant of time. The bottom panel of Figure 3 displays an example of the fitting for a instant of time for 29 March 2011. We typically used image triplets from STEREO COR1 and COR2 in combination with SOHO/LASCO-C2, except for two cases in which we also used LASCO-C3 because the CME quickly leaves the LASCO-C2 FOV. The obtained GCS parameters of latitude, longitude, and height of the CME apex, added to those measured using the triangulation technique on the prominence, are useful to analyze the spatio-temporal evolution of both structures.

2.3. Magnetic Energy Density Maps

To analyze the relationship between prominence/CME deflection and the magnetic environment, i.e. how the surrounding coronal conditions affect the trajectory of both structures, we compute maps of energy density associated with the magnetic field $[B]$. The magnetic-energy density ($\propto B^2$) distribution at different heights is determined from the potential-field source-surface (PFSS) model by Schrijver and De Rosa (2003).

This model uses a photospheric magnetic-field value derived from magnetograms and, adopting a potential-field approximation, it extrapolates its value to other heights, between $1\,\mathrm{R}_\odot$ and $2.5\,\mathrm{R}_\odot$. A magnetogram taken at the time of the prominence-eruption onset together with a static PFSS extrapolation were used for each event. The magnetic-energy density-distribution enables an estimation of the local magnetic gradient to determine the possible influence of the magnetic field on the trajectory of the prominences and CMEs. However, this technique does not consider the magnetic energy associated with the eruption. The PFSS 3D extrapolations are also used to examine the global magnetic field and to search for the presence of magnetic structures such as coronal holes, helmet streamers, and/or pseudo-streamers in the vicinity of each source, erupting prominence, and CME. Figure 4 shows an example of magnetic-energy-density maps for 29 March 2011 at different heights. The iso-contours (in logarithmic scale) over-plotted on top of the (gradient-filled) gray background indicate levels of constant B^2 (as indicated by the iso-contours, darker

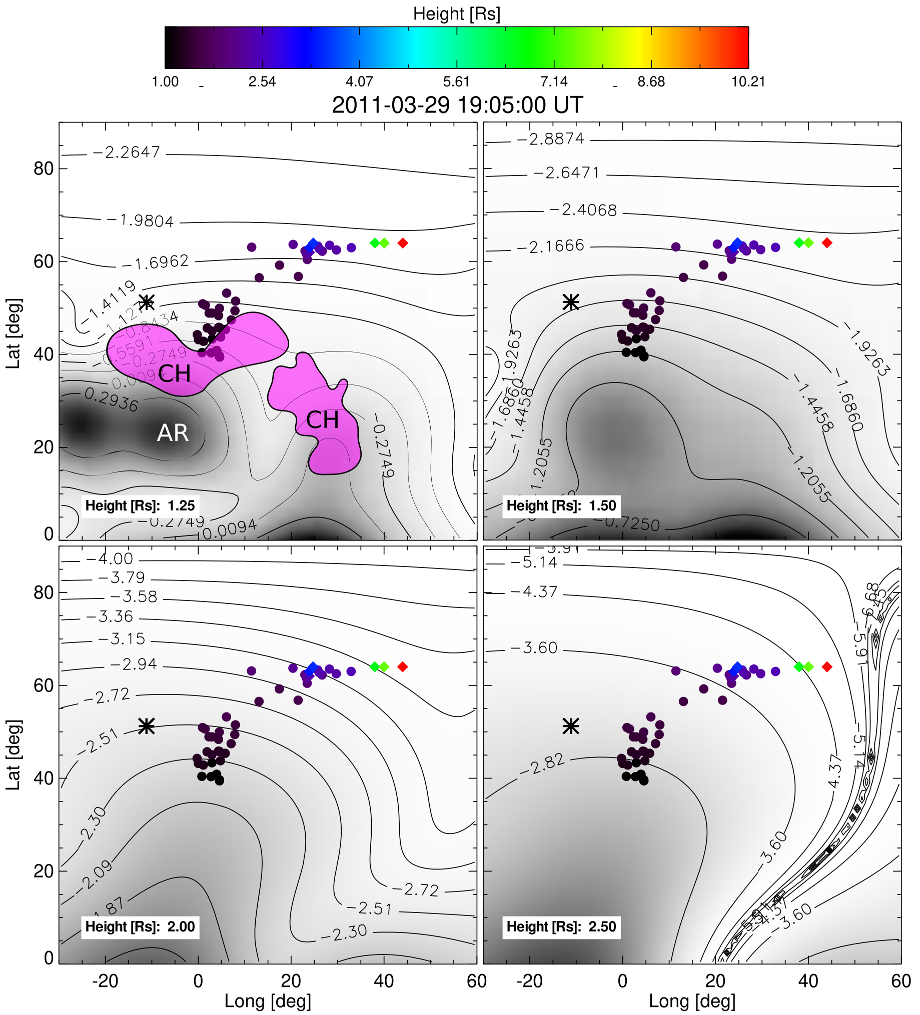

Figure 4 Magnetic-energy-density maps at different heights for the event that occurred on 29 March 2011. The corresponding height is indicated in the bottom-left corner of each panel. The gray scale represents the intensity of the magnetic energy, where the darker regions represent higher intensity. The contours (solid-black lines) indicate also the magnetic energy on logarithmic scale. In the map corresponding to $2.5\,R_\odot$ the HCS is delimited by a thick-black curve. The magenta filled contours in the first panel denote the coronal holes (CH) obtained from EUV images and the active regions are pointed with AR. The black asterisk represents the central position of the source region. The filled circles show the coordinates obtained from the tie-pointing technique for the prominence and the diamond-shaped symbols show the measurements obtained with GCS model for the CME. The color of each symbol indicates its height according to the color key at the top.

regions correspond to higher magnetic-energy values). The time of the magnetogram considered for the PFSS extrapolation is indicated at the top of Figure 4. The black asterisk represents the central position of the source region, the circles indicate the triangulated prominence points and the diamond-shaped symbols show the coordinates obtained from the GCS model of the CME. The color of the symbols indicates the height. At lower heights (top panels) we can see localized structures as active regions (AR), to the South of the measured points, and two coronal holes (CH), also to the South. As the height increases (bottom panels), the global structure of the magnetic field becomes evident including the HCS. Note from the contour levels, that the intensity of the magnetic field decays at least two orders of magnitude within the height range considered.

2.4. Trajectory in the Θ–Φ Plane and Gradient of Magnetic Energy Density

In this section we examine the effect of the magnetic field in deflecting the investigated structures, i.e. both erupting prominence and CME, by analyzing their 3D trajectory in the context of the magnetic configuration, which is provided by magnetic-energy-density maps. Specifically, from these maps we calculate the direction of the local magnetic-pressure force for each 3D coordinate, but we do not quantify the magnetic tension force. From the variability of latitude and longitude with time and height, it is possible to plot the trajectory projected in the latitude vs. longitude plane (Θ–Φ plane). As a first step, we plot latitude and longitude as a function of height, as in the example displayed in the top panels of Figure 5. The different symbols are measurements resulting from the various instruments, while their color coding represents height. Data series "TRIANG AIA–EUVI" and "TRIANG SWAP/EUVI" denote triangulations of prominence parcels performed in the low corona. Additionally, note that the data series "TRIANG COR1" corresponds to parcels of the prominence identified in the CME core and tracked in the COR1-A and -B coronagraphs; whereas "GCS" data series refer to the CME apex. Solid lines represent fits applied to the latitude and longitude coordinates as a function of height. In this event, a quadratic fit is implemented for the filament data and a linear fit for the CME measured points. We use linear or quadratic functions according to the behavior of the prominence and CME for each event. We do not include the source in the prominence fit because this measurement corresponds to a different part of the triangulated filament.

The bottom panel of Figure 5 displays the resulting trajectory of both data series projected onto the Θ–Φ plane. Vectors tangent to the curve, described by $\mathrm{d}\Theta/\mathrm{d}\Phi = (\mathrm{d}\Theta/\mathrm{d}h)/(\mathrm{d}\Phi/\mathrm{d}h)$, are plotted as cyan arrows for several points over the fitted trajectory. At the location of these points we also calculate the direction of the gradient of magnetic-energy density computed from the magnetic-density maps; see Figure 4. The direction of the magnetic gradient is displayed with red arrows. It can be assumed that the magnetic field becomes predominantly radial for heights above $2.5\,\mathrm{R}_\odot$, in which case the magnetic-energy density would change only in the radial direction, and not in the Θ–Φ plane. Therefore, for heights above $2.5\,\mathrm{R}_\odot$ gradients are assumed to keep the same direction. The length of the cyan and red arrows are scaled to have comparable sizes for visualization purposes, hence they do not represent the actual magnitude of the tangent and the magnetic gradient. To quantify whether the trajectory is aligned with the direction of the magnetic gradient, we determine the angle between these two vectors. These results are shown in Section 3.1.

3. Results

With the aim of performing a systematic study of CMEs having large deflections, we focus the analysis on the main sources of deflection previously studied by other authors (e.g. Gui et al., 2011; Liewer et al., 2015; Kay, Opher, and Evans, 2015): the influence of the magnetic force and the kinematic features of both structures – prominence and associated CME.

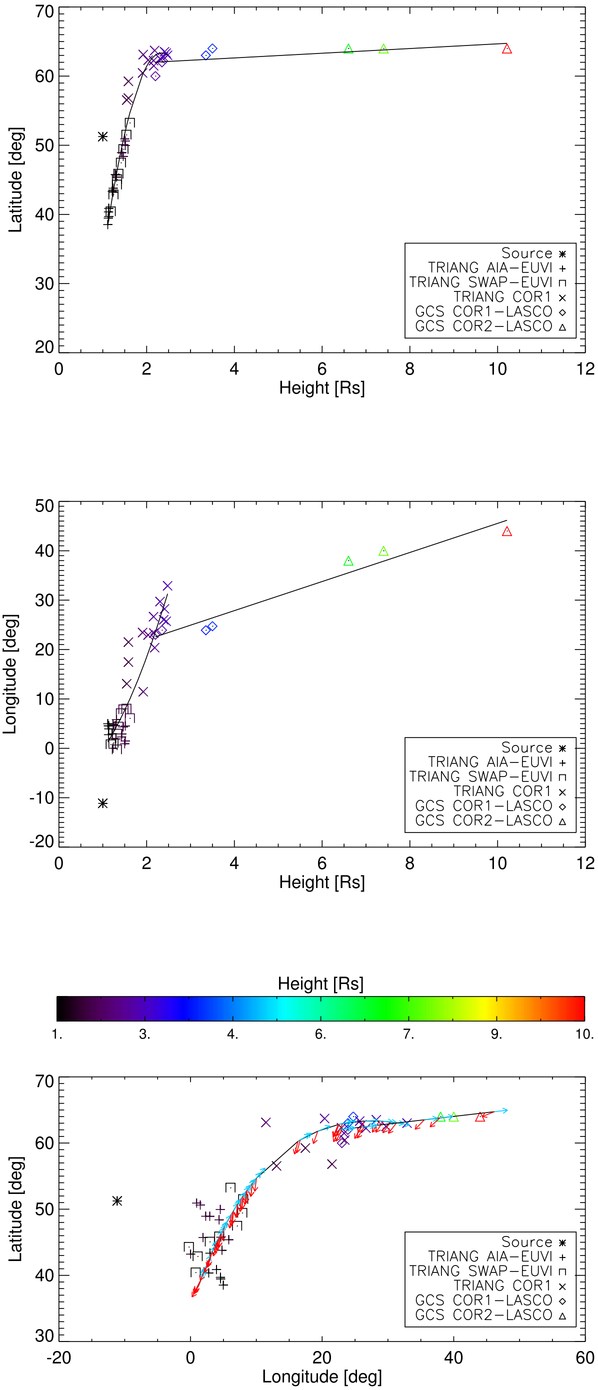

Figure 5 Top and middle panels: Latitude and longitude, respectively, as a function of height for the event on 29 March 2011. The various symbols indicate the measurements of the coordinates using different methods and imagers. The solid-black lines correspond to a quadratic fit applied to the prominence data and a linear fit applied to the CME data series. Bottom panel: Trajectories (black solid lines) projected on the Θ–Φ plane resulting from the fitted curves. Cyan arrows represent the direction of the tangent vector and red ones show the direction of the magnetic-energy-density gradient. The color scale of the measured points indicates their height.

3.1. The Role of the Magnetic Environment on Deflection

The measured coordinates of source region, prominence parcels, and CME apex plotted as symbols on synoptic maps of magnetic-energy density (built as explained in Section 2.3), allow us to comprehensively visualize the location of the various structures. Given their significance, in Figure 6 we show all resulting plots for the 13 analyzed events considering the magnetic-energy maps obtained from the PFSS extrapolation model with the source surface at $2.5\,\mathrm{R}_\odot$. The times of the magnetograms used for the PFSS extrapolations are indicated in each panel. The gray background shows the intensity of the magnetic energy, with darker regions having the highest magnetic energy and brighter regions associated with lower magnetic energy. The HCS is indicated with a thick-solid-black line and the other solid-black lines represent contour levels of the magnetic energy. The reconstructed points are displayed as colored circles for the prominence and colored diamonds for the CME, with black representing the lowest height ($1\,\mathrm{R}_\odot$) and red the greatest ($15\,\mathrm{R}_\odot$) of all events. The source is indicated with a black asterisk. The fitted trajectories are indicated with yellow lines superimposed on the reconstructed points. It can be appreciated how trajectories evolve in some cases by moving away from regions of high magnetic-energy density and in other cases heading towards regions of low magnetic-energy density. A quantitative way of evaluating such a behavior can be achieved by determining the angle between the tangent direction to the trajectory and the gradient of magnetic-energy density, as described in Section 2.4. Henceforth we will call this angle δ. Ideally, ejecta moving directly towards the HCS or a local minimum energy region and away from high magnetic-energy regions, i.e. against the gradient of magnetic-energy density, would present an angle $\delta \approx 180^\circ$.

In the top panel of Figure 7 we show the distribution of δ as determined from each and every measured point of all events. To have an equal number of points in the same height range for all events, we have interpolated the fitted trajectories obtained in Section 2.4 from 1 to $2.5\,\mathrm{R}_\odot$ for prominence measurements and from 2.5 to $4\,\mathrm{R}_\odot$ for CME reconstructed values. The results obtained from filament parcels from 1 to $2.5\,\mathrm{R}_\odot$ are shown with a black-solid line, while the magenta-dashed line represents the angular distribution for CME measurements from 2.5 to $4\,\mathrm{R}_\odot$. The vertical dotted lines indicate values of 60° and 120° for δ. For lower heights ($<2.5\,\mathrm{R}_\odot$) δ shows a flattened distribution for prominences, with 53% of the values distributed between 120° and 180°, while 30% present values between 60° and 120° and the remaining 17% show smaller angles. For greater heights, between 2.5 and $4\,\mathrm{R}_\odot$, the δ-distribution for CMEs measurements is less-dispersed. Approximately 69% of the values are between 120° and 180° (of which 38% are concentrated between 160° and 180°), 22% of the present values between 60° and 120°, and the remaining 9% show lower angles. In general, it can be said that the values of δ for altitudes $<2.5\,\mathrm{R}_\odot$ fluctuate more than the values for altitudes $>2.5\,\mathrm{R}_\odot$. This suggests that the alignment of the direction of deflection with the direction in which the magnetic-energy decreases takes place more often at higher altitudes ($>2.5\,\mathrm{R}_\odot$).

In order to inspect the contribution of each event to the δ-distribution, both the spread of the δ-measurements and the mean values for each event are shown in the bottom panel of Figure 7 (the x-axis indicates the event ID from column 1 of Table 1). For each event, we have calculated the mean value of the angle δ for the prominence (black squares) from 1 to $2.5\,\mathrm{R}_\odot$, and for the CME (magenta diamonds) from $2.5\,\mathrm{R}_\odot$ to $4\,\mathrm{R}_\odot$. The respective standard deviations are represented by the vertical lines centered on the measurements (note that, for the CME measurements, they are of the order of the symbol size in the plot). The horizontal dotted lines denote the same values of δ indicated in the top panel, 120° (upper line) and 60° (lower line). Note that the spread of the measurements is much larger for prominences

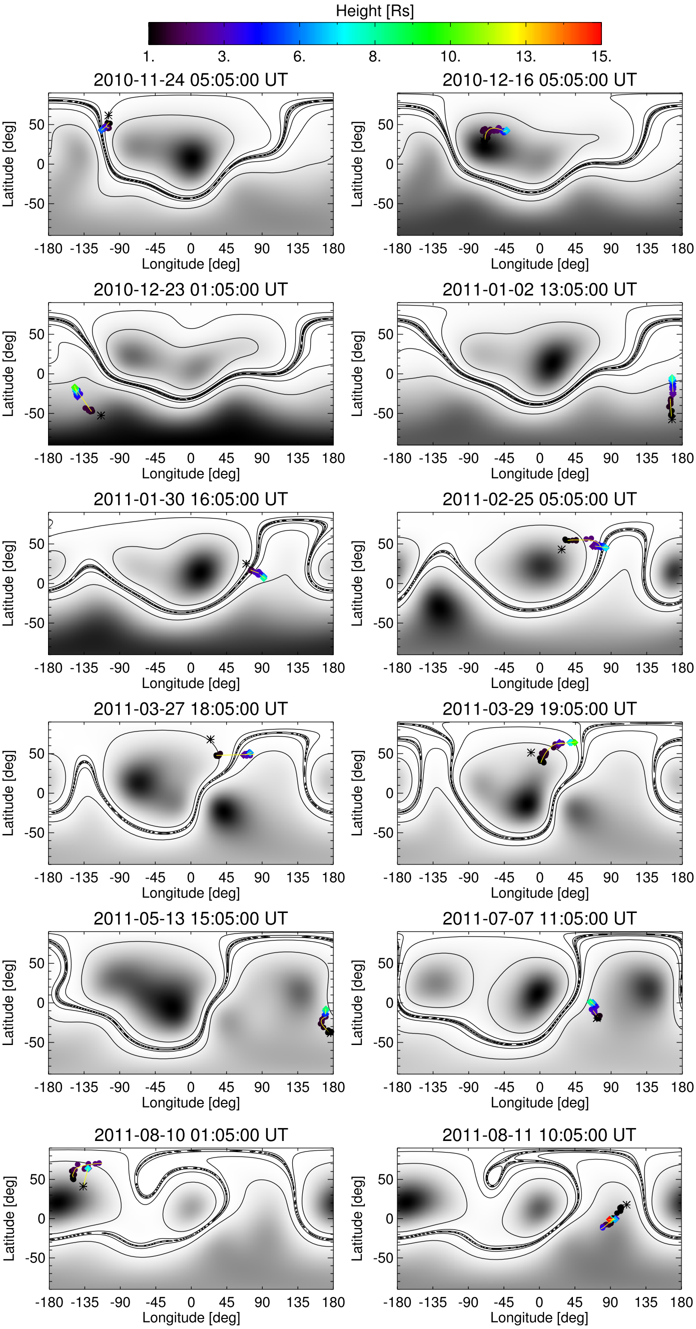

Figure 6 Synoptic maps of magnetic-energy density (gray-scale shaded background) at 2.5 $R_\odot$ for ten dates of the 13 events in Table 1. Solid-black lines are contours of low magnetic-energy density. The thick–solid-black line indicates the HCS. The colored dots represent the coordinates of tracked prominence parcels and diamond-shaped points indicate the CME apex, with the color coding representing their height. The dots and the diamonds are connected by yellow lines, which represent the fitted trajectory. The source region is indicated with a black asterisk.

Figure 6 (*Continued*)

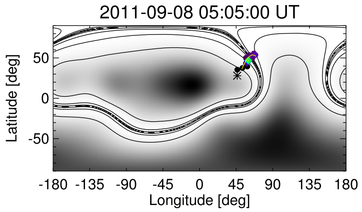

than for CMEs. This is in agreement with the flattened distribution obtained for prominence measurements and the less-dispersed CME distribution shown in the top panel.

By looking into each individual case, we find that the prominences with mean values of δ between 120° and 180° are related to erupting filaments that have nearby ARs and CHs on the same side and opposite to the direction of deflection. This suggests that they could be deflected by the combined action of both structures. These events are 16 December 2010, 23 December 2010, 2 January 2011, 25 February 2011, 29 March 2011, and 10 August 2011. The rest of the prominences (24 November 2010, 30 January 2011, 27 March 2011, 13 May 2011, 07 July 2011, 11 August 2011, and 08 September 2011) are close to only one of these structures, either CHs or ARs, or both of them are present but not on the same side. The CMEs with mean δ between 120° and 180° leave the low corona near the HCS

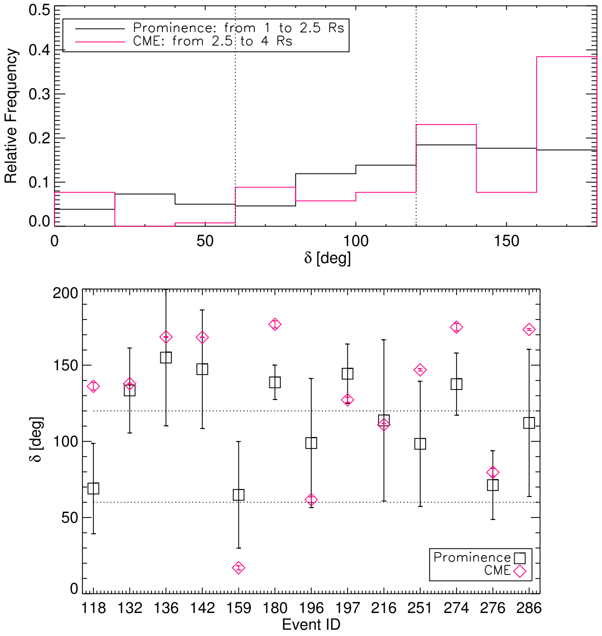

Figure 7 Top panel: Distribution of δ (angle between the trajectory tangent and the gradient of the magnetic-energy) corresponding to the two analyzed structures. The distribution of the angle for filament parcels is shown with a black-solid line considering the fitted curves from 1 to 2.5 $R_\odot$. For the CME this angle is considered between 2.5 to 4 $R_\odot$ and is shown with a magenta-dashed line. The vertical dotted lines define the three intervals of values considered for the interpretation. Bottom panel: Mean values and standard deviations of δ for prominences (black squares) and CMEs (magenta diamonds) for each event. The event ID corresponds to the ID from the *AIA Filament Eruption Catalog* indicated in Table 1. The same intervals considered in the top panel are indicated here with horizontal dotted lines.

or a region of low magnetic energy, moving away from CHs. This would indicate that the direction of the trajectory of most CMEs is opposite to the direction of maximum magnetic-energy growth, in agreement with previous reports (e.g. Gui et al., 2011). All CMEs that show $\delta < 120°$ (30 January 2011, 27 March 2011, 13 May 2011, and 11 August 2011) are described in detail in Section 3.3.

To gain further insight into the properties of CME deflections, we performed a kinematic study of prominences and CMEs described in the following section.

3.2. Kinematic analysis

With the aim of studying the relationship between propagation speed and deflection, we determined the 3D velocity of prominences and CMEs for all events. By applying the tie-pointing method to the apex of the prominence material and by fitting CMEs with the GCS model, both at different times, we obtained 3D coordinates as described in Section 2.2. We determined the radial- and transverse-propagation speed of prominences and CMEs by implementing quadratic or linear fits to the respective coordinate vs. time data. Figure 8 shows the resulting radial speeds as a function of height for prominences (left) and CMEs (right) for each event. Although the propagation of these events is non-radial, particularly at lower heights, we prefer to show the radial component of the velocity because the comparison with previous studies is straightforward (this is the component usually reported). Nevertheless, for a more comprehensive analysis, we also show the magnitudes of the transverse speed, i.e. the component of the velocity parallel to the Sun's surface, in Table 2. The first two columns show the event ID and the date of the event, as in Table 1. Columns 3 – 5 indicate the radial [v_r] and transverse [$v_\perp$] components and 3D magnitude [v] of the prominence velocity at $2.5\,\mathrm{R}_\odot$. Columns 6 – 8 display the respective values of CME speed at $5\,\mathrm{R}_\odot$. We display speed values at these heights because they are representative of the evolved prominences and CMEs, respectively. Note that 3D speeds are almost equal to the radial component, especially for CMEs, where the transverse components are negligible compared to the radial. However, for some of the prominences, the transverse component is comparable to the radial one. Note from Figure 8 that all prominences exhibit accelerated radial-speed profiles, with most of the events reaching values of 500 $\mathrm{km\,s^{-1}}$, except for one event that reaches 1500 $\mathrm{km\,s^{-1}}$. CMEs have values about 1000 $\mathrm{km\,s^{-1}}$ with some of the events showing no acceleration, presumably because most of it took place at lower heights.

In addition, we have computed the 3D deflection [$\Psi(h)$] with respect to the source region at different heights for both prominences and CMEs. We fit an exponential function of the form $p_0 - p_1 \exp(-p_2 x)$ to the deflection as a function of height $\Psi(h)$ using a different set of parameters for prominences and CMEs, given that in general the deflection profiles of both structures differ, and they do so for each event. This function describes well the general behavior of the measurements, i.e. a rapid increase at lower heights and a flatter trend at higher ones.

The deflection rate with height, calculated as $\mathrm{d}\Psi/\mathrm{d}h$, is shown in logarithmic scale in Figure 9. The deflection rate for prominences (left panel) decreases abruptly, one order of magnitude for heights lower than $2\,\mathrm{R}_\odot$ for most of the events (except for events on 23 December 2010, 2 January 2011, and 30 January 2011, whose deflection rates are almost constant). In contrast, the deflection rate for CMEs (right panel of Figure 9) decreases less steeply, one order of magnitude for heights lower than $4\,\mathrm{R}_\odot$ (except for events on 27 March 2011 and 10 August 2011, which rapidly decay). Calculating the mean height where deflection rates decay $1/\mathrm{e}$ of their initial values (h_e hereafter) results in $2.3\,\mathrm{R}_\odot$ for prominences

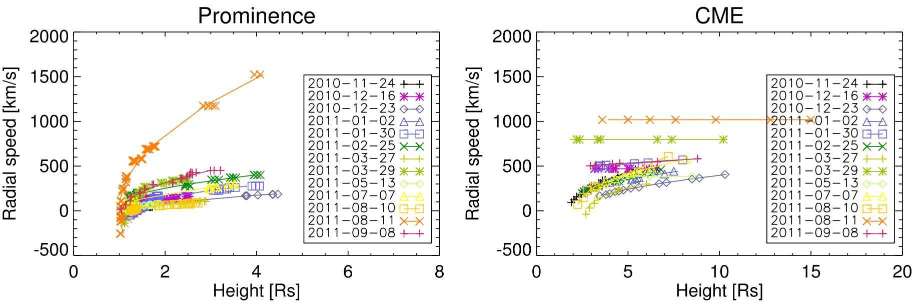

Figure 8 Radial propagation speed of prominences (left) and CMEs (right) as a function of height. The different colors and symbols indicate different events.

Table 2 Magnitudes of radial, transverse, and 3D speeds for prominences and CMEs for each event. The first two columns display the *AIA Filament Eruption Catalog* ID and the corresponding date of the event. Columns 3 – 5 show the prominence radial [v_r], transverse [$v_\perp$], and 3D speed [v], respectively, calculated at 2.5 $R_\odot$. Columns 6 – 8 exhibit the same components of CME speed evaluated at 5 $R_\odot$. All of the speed values are presented in $\mathrm{km\,s^{-1}}$.

Catalog		Prominence speed at 2.5 $R_\odot$			CME speed at 5 $R_\odot$		
ID	Date	v_r	$v_\perp$	v	v_r	$v_\perp$	v
(1)	(2)	(3)	(4)	(5)	(6)	(7)	(8)
118	24 Nov 2010	65	82	105	435	83	443
132	16 Dec 2010	173	73	188	470	92	479
136	23 Dec 2010	115	35	120	241	20	242
142	02 Jan 2011	97	28	102	351	2	351
159	30 Jan 2011	191	48	197	523	32	524
180	25 Feb 2011	296	81	307	371	86	381
196	27 Mar 2011	93	93	131	256	27	258
197	29 Mar 2011	384	210	438	796	187	818
216	13 May 2011	104	106	148	384	7	384
251	07 Jul 2011	227	47	232	407	69	413
274	10 Aug 2011	80	59	99	456	2	456
276	11 Aug 2011	1052	324	1101	1018	250	1049
286	08 Sep 2011	389	75	396	534	23	534

and 2.4 $R_\odot$ for CMEs. This suggests that most of the deflection with respect to the source region occurs below 2.4 $R_\odot$.

To analyze in further detail the deflection rate of prominences, we show in Figure 10 (left panel) the deflection rate at a height h_e against the radial propagation speed at 2.5 $R_\odot$. Each event is represented by a different color. Note that in general slower prominences show deflection rates greater than 20°, while faster events present deflection values lower than 20° (except 11 August 2011).

Following the line of Gui et al. (2011), we also inspect a possible dependence between the deflection rate and the magnitude of the magnetic gradient at each latitude–longitude coordinate. Figure 10 (right panel) displays results arising from the prominence analysis. We found a correlation of 0.65, which suggests a moderate linear relationship

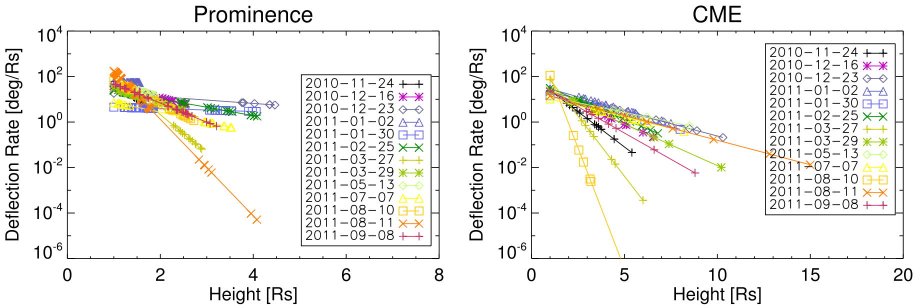

Figure 9 Deflection rate vs. height for prominences (left) and CMEs (right). The different colors and symbols indicate different events.

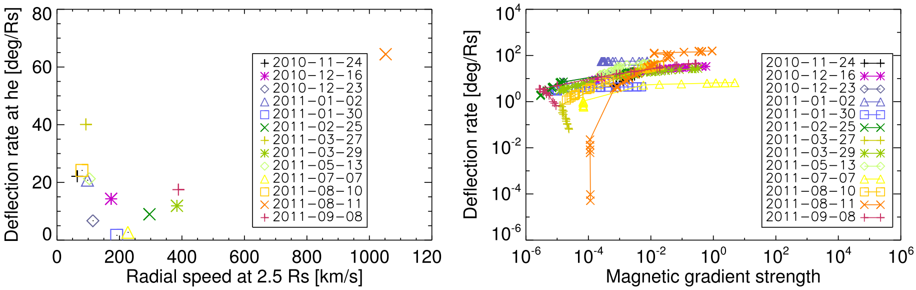

Figure 10 Left panel: Prominence deflection rate at the height where this quantity decays at $1/e$ of its initial value [h_e] vs. radial propagation speed at $2.5\,R_\odot$. Right panel: Prominence deflection rate as a function of the magnitude of the magnetic gradient. The color pattern indicates different events in both panels.

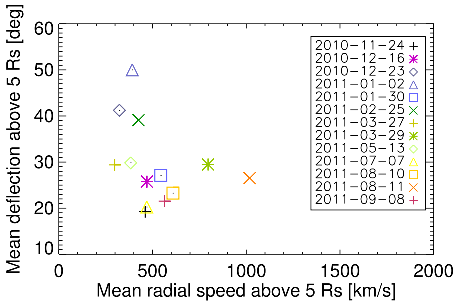

Figure 11 Total CME deflection as a function of CME speed, both averaged for heights greater than $5\,R_\odot$.

between the deflection rate for prominences and the strength of the magnetic gradient. For CMEs we do not perform this analysis because we consider unchanged density maps for heights greater than $2.5\,R_\odot$, hence the gradient keeps its value from this height outward.

For the case of CMEs, we computed the mean total 3D deflection with respect to their source regions at heights greater than $5\,R_\odot$, since the deflection stabilizes around that height. This overall 3D deflection is compared with the mean radial speed, also averaged for heights greater than $5\,R_\odot$, in Figure 11. Two groups can be distinguished in the figure: CMEs that

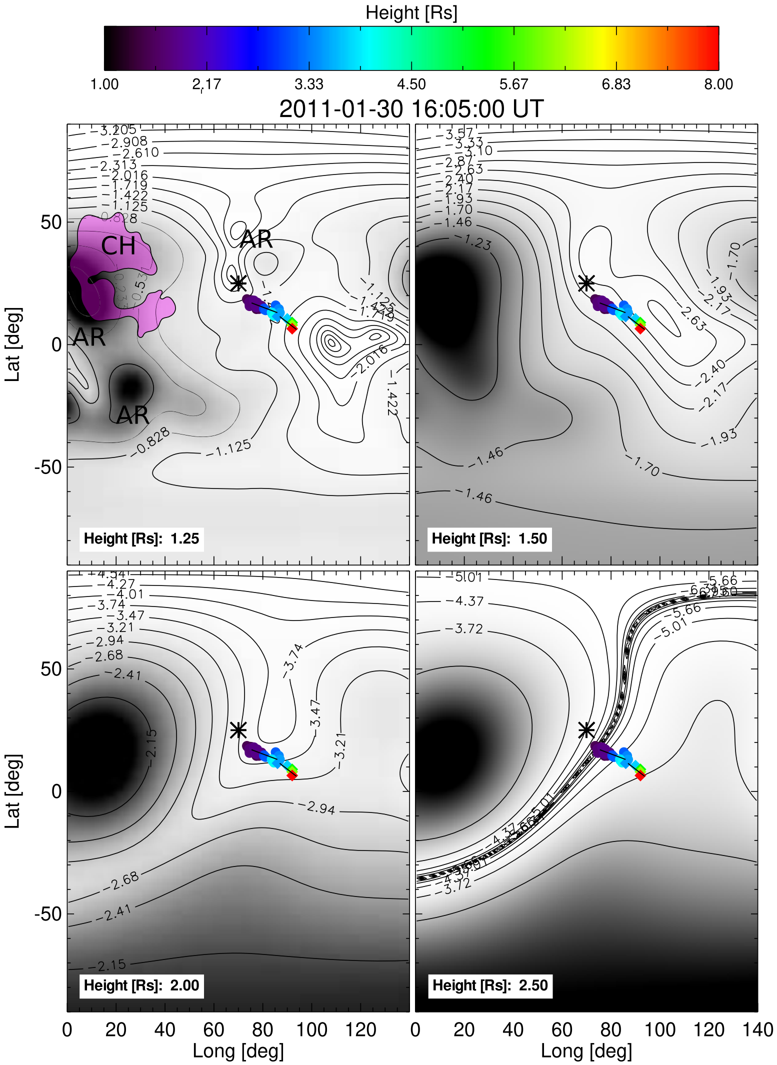

Figure 12 Magnetic-energy-density maps at different heights for the event that occurred on 30 January 2011. The corresponding height is indicated at the bottom-left corner of each panel. The gray scale represents the intensity of the magnetic energy, where the darker regions indicate higher intensity. Contours (solid-black lines) indicate magnetic-energy values on a logarithmic scale. The magenta-shaded area represents the location of a CH obtained from EUV images. The black asterisk represents the central position of the source region. The circle-shaped points represent prominence coordinates and the diamond-shaped correspond to CME coordinates. The color scale of the measured points indicates their corresponding height. The solid-black lines superimposed on the colored points are the fitted trajectories.

have speeds lower than $\approx 450\ \mathrm{km\,s^{-1}}$ present total deflections greater than 30°; and CMEs with speeds greater than $\approx 450\ \mathrm{km\,s^{-1}}$ exhibit deflection values lower than 30°. This suggests that CMEs having speeds greater than the slow solar-wind speed deflect less than slower ones.

To summarize, the major deflection occurs at heights below $2.4\,\mathrm{R}_\odot$ in the prominence domain. The deflection rate of prominences apparently is related with their propagation speed and the strength of the magnetic gradient. The total deflection with respect to the source region is presumably influenced by the CME speed relative to the slow solar-wind speed and the direction of the magnetic-field gradient.

3.3. Qualitative analysis of events with low δ

Cases for which the mean angle [δ: angle between the trajectory and magnetic-energy gradient, see bottom panel of Figure 7] for CMEs is below 120° do not follow the general trend and thus are worthy of a deeper analysis. These events are: 30 January 2011, 27 March 2011, 13 May 2011, and 11 August 2011. In the following we summarize the qualitative findings.

3.3.1. Events on 30 January 2011 and 27 March 2011

The CMEs on 30 January 2011 and 27 March 2011 propagate both beyond the HCS resulting in $\delta < 90^{\circ}$. Figure 12 displays the magnetic-energy-density maps at different heights for the event on 30 January 2011. The background gray scale represents values of magnetic-energy density, where darker regions have higher strength. The colored circles and diamond-shaped points indicate prominence and CME measured coordinates, respectively, at various heights, while the asterisk represents the source region. Active regions and coronal holes are denoted by AR and CH, respectively. The area of the CH, obtained from EUV images, is shaded in magenta in the first map. The source region is near an AR to the North and the measured coordinates of the prominence indicate that it is first deflected toward a local magnetic-energy minimum at heights lower than $1.25\,\mathrm{R}_{\odot}$ (first panel of Figure 12). The second and third panels (1.5 and $2.0\,\mathrm{R}_{\odot}$, respectively) show that the prominence is later deflected away from the northern and eastern ARs and from the CH. Note that the CME is also moving away from these structures and follows the same initial direction. At $2.5\,\mathrm{R}_{\odot}$ (last panel) the CME trajectory is seen beyond the HCS. On this event the influence of the magnetic-energy minimum at low heights seems to be crucial for the following evolution of the structures. Also it is important to mention that there is another CME to the East that is already propagating and could influence the trajectory of the CME analyzed in this work.

The initial evolution of 27 March 2011 is different. In the early stages, the prominence moves southward towards a CH (see first panel of Figure 13) and away from open magnetic-field lines located near the North Pole. Then, at higher altitudes, the prominence deflects abruptly to the West moving away from the CH (second and third panel of Figure 13), crossing the assumed location of the HCS between $1.35\,\mathrm{R}_{\odot}$ and $2.3\,\mathrm{R}_{\odot}$. Thus, the CME is originating beyond the HCS and its trajectory is not aligned with the magnetic-energy gradient resulting in $\delta < 90^{\circ}$.

As mentioned before, both of these events do not follow the path of minimum magnetic energy. In the first event the influence of the magnetic forces at low heights seems to be strong enough to push the CME beyond the HCS, in agreement with findings on some events described by Kay, Opher, and Evans (2015). In the second case the prominence is strongly deflected at higher altitudes by the magnetic tension of a CH. This structure does not produce a magnetic-gradient variation, but it would rather represent a magnetic wall that the CME is not able to penetrate, presumably because of its low speed.

3.3.2. The 13 May 2011 event

This event shows a different behavior compared to 30 January 2011 and 27 March 2011. From the first panel of Figure 14 we note that the prominence is located be-

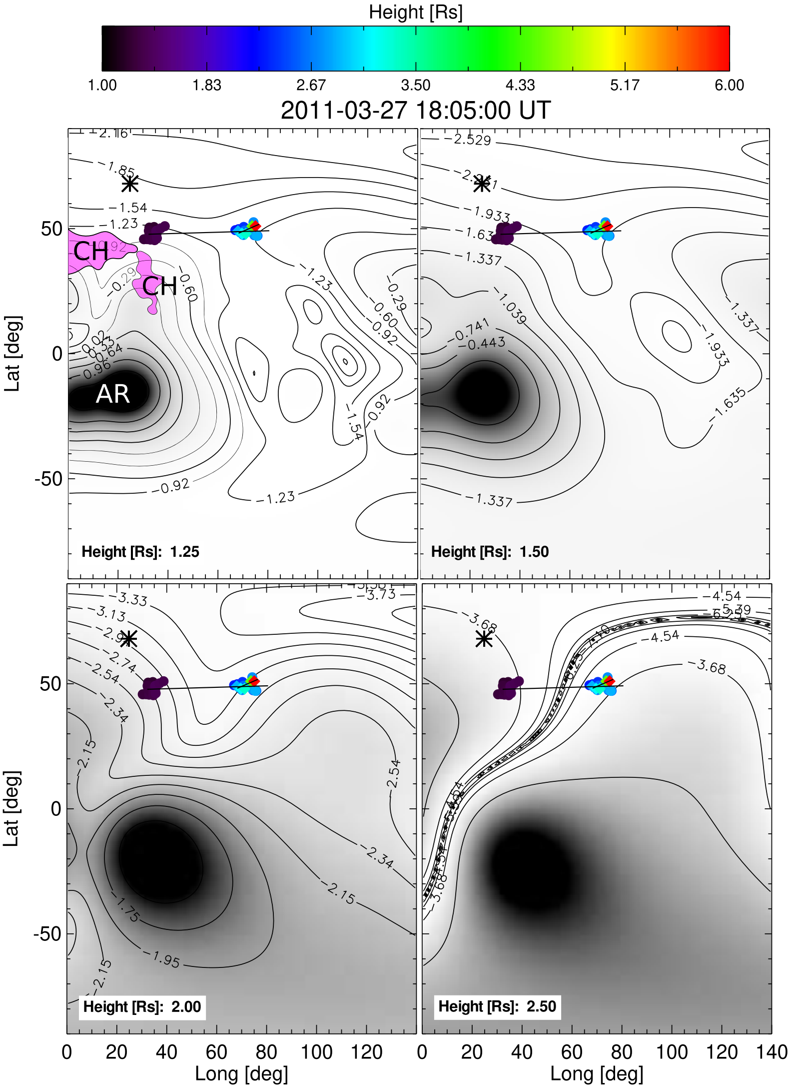

Figure 13 Magnetic-energy-density maps at different heights for the event that occurred on 27 March 2011. The corresponding height is indicated at the bottom-left corner of each panel. The gray scale represents the intensity of the magnetic energy and the contours (solid-black lines) indicate magnetic-energy values on a logarithmic scale. The magenta-shaded area represents the location of a CH obtained from EUV images. The color scale of the measured points indicates their corresponding height. The black asterisk represents the central position of the source region. The circle-shaped points represent prominence coordinates and the diamond-shaped correspond to CME coordinates. The solid-black lines superimposed on the colored points are the fitted trajectories.

tween a southern CH and a northern AR. There are also other magnetic structures surrounding the prominence: an arm of the CH located to the East between approximately −50° and −20° in latitude, and an AR and a pseudostreamer (PS) located to the West. The first and second panels of Figure 14 show that the initial trajectory of

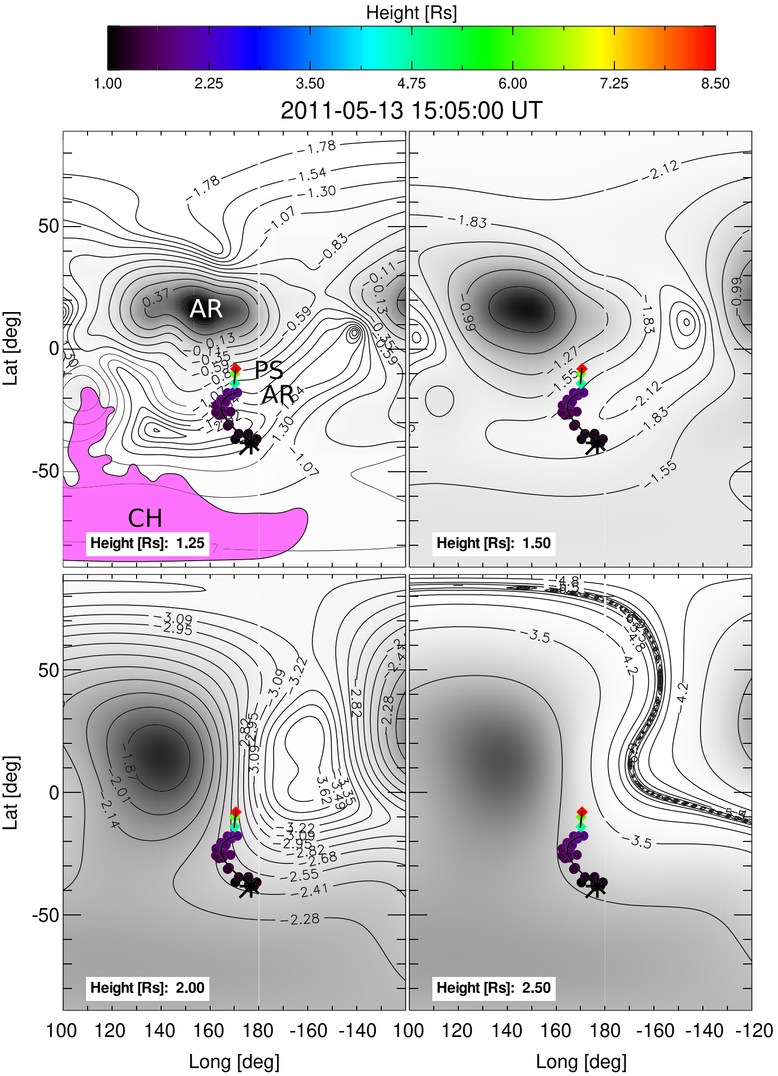

Figure 14 Magnetic-energy-density maps at different heights for the event that occurred on 13 May 2011. The corresponding height is indicated at the bottom-left corner of each panel. The gray scale represents the intensity of the magnetic energy, where the darker regions indicate higher intensity. Contours (solid-black lines) indicate magnetic-energy values on a logarithmic scale. The magenta-shaded area represents the location of a CH obtained from EUV images. The circle-shaped points represent prominence coordinates and the diamond-shaped correspond to CME coordinates. The color scale of the points indicates their corresponding height. The solid-black lines superimposed on the colored points are the fitted trajectories. The black asterisk represents the central position of the source region.

the prominence is influenced by a local minimum of magnetic energy, until $1.5R_{\odot}$, and then it deflects towards lower magnetic-energy region (third and fourth panel). Above $1.5\,R_{\odot}$, the CME moves away from the CH, presumably in an attempt to head toward regions of low magnetic energy, but it is confined by the mentioned structures.

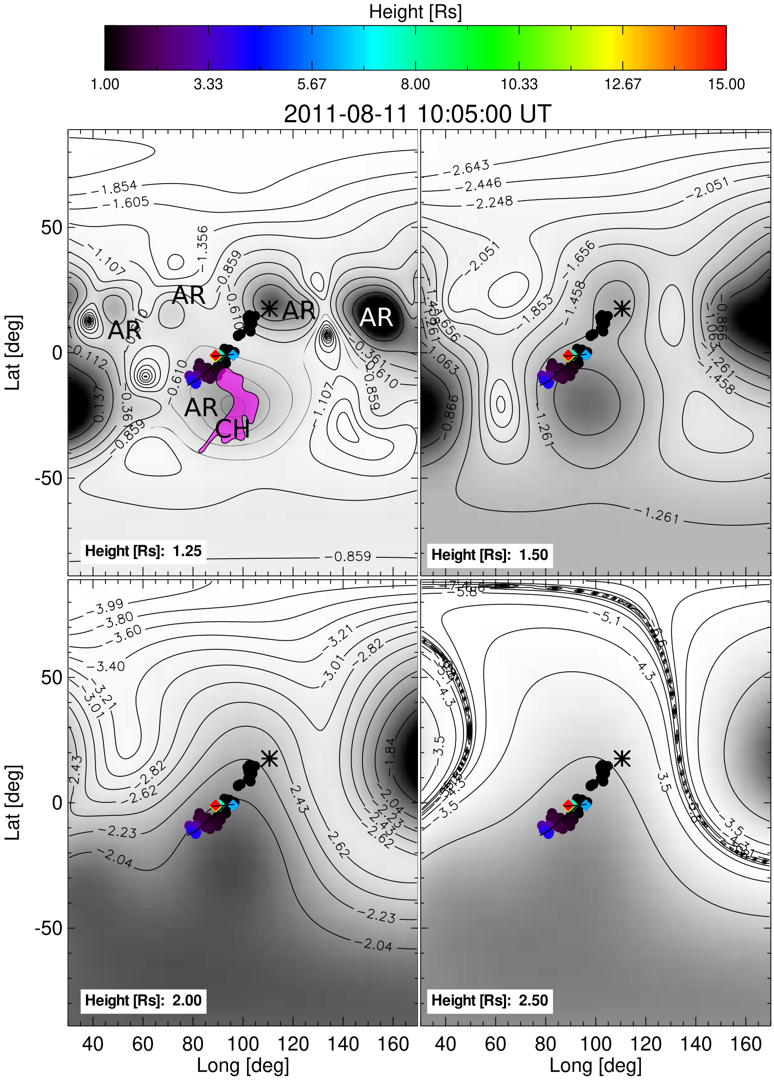

Figure 15 Magnetic-energy-density maps at different heights for the event that occurred on 11 August 2011. The corresponding height is indicated at the bottom-left corner of each panel. The gray scale represents the intensity of the magnetic energy, where the darker regions indicate higher intensity. Contours (solid-black lines) indicate magnetic-energy values on a logarithmic scale. The magenta-shaded area represents the location of a CH obtained from EUV images. The circle-shaped points represent prominence coordinates and the diamond-shaped correspond to CME coordinates. The color scale of the points indicates their corresponding height. The solid-black lines superimposed on the colored points are the fitted trajectories. The black asterisk represents the central position of the source region.

3.3.3. The 11 August 2011 event

As we note from the first and second panels of Figure 15, the source region of the 11 August 2011 event is an AR, and for altitudes below 1.5 $R_\odot$ the prominence trajectory is directed towards a local minimum of the magnetic energy, moving away from the northern AR but approaching a southern CH and an AR. This produces a deflection mainly in the latitudinal direction. At altitudes greater than 3.6 $R_\odot$ the CME abruptly moves towards the eastern HCS (fourth panel at 2.5 $R_\odot$) but not in the direction of maximum decrease of magnetic energy. This happens probably due to its high kinetic energy, given that its velocity is 1160 $\mathrm{km\,s^{-1}}$, which adds to the magnetic tension produced by the southern CH.

4. Discussion and Conclusions

We have performed a systematic analysis of large CME deflections within a period of a year (October 2010 – September 2011) in the rising phase of Solar Cycle 24. We found 13 events that deflect more than 20° from their source regions. Inspired by previous reports (e.g. Gui et al., 2011; Liewer et al., 2015; Kay, Opher, and Evans, 2015) we carried out a detailed investigation on the allegedly principal causes of deflection: the influence of background magnetic forces and kinematic features. We examined these aspects from the beginning of the eruptions, studying the evolution of CMEs and their associated prominences.

To shed light on the role of these aspects, we have defined an angle [δ] that represents the angular span between the orientation of the trajectory of both structures and the direction of magnetic-energy-gradient related to the magnetic pressure force. For prominences this angle shows a dispersed behavior, with half of the values (obtained from the measurements of all events between 1 – 2.5 $R_\odot$) greater than 120° (see top panel of Figure 7). This means that, for half of the triangulated coordinates, the direction of the trajectory is aligned with the direction of magnetic-energy gradient decrease. By inspecting each event, we notice that half of them exhibit mean δ-values greater than 120° (see bottom panel of Figure 7). Nonetheless, the deflection rate of prominences appears to be proportionally related with the magnetic-gradient strength, since the higher the gradient, the larger the deflection rate. This could be attributed to the fact that the magnetic structure at lower heights is more complex, with high field intensity and no large-scale structures present to affect the prominence trajectory. Other possible reasons are that the intrinsic magnetic field of the prominence and flux rope would be more intense than the surrounding magnetic structures, and also reconnection topologies and processes that are beyond the scope of this study. As a consequence of stronger magnetic fields at low altitudes, the deflection rates are larger for prominences than for CMEs, also supported by the correlation found between deflection rate and magnetic-gradient strength. The obtained mean h_e (the mean height where deflection rates decay 1/e of their initial values) resulting in 2.3 $R_\odot$ for prominences and 2.4 $R_\odot$ for CMEs, also suggests that most of the deflection with respect to the source region occurs below 2.4 $R_\odot$. The kinematic analysis also sustains this result since some prominences exhibit a transverse component of velocity (parallel to the Sun's surface) at 2.5 $R_\odot$ comparable or greater than the radial one, while at larger heights CMEs exhibit comparably smaller values of transverse speed. This study also revealed a tendency for slower events to have larger deflection rates (namely $> 20^\circ\,R_\odot^{-1}$).

For CMEs we found that $\approx$70% of δ-values correspond to trajectories that follow directions opposite to the magnetic gradient and most of the CMEs propagate towards the minimum energy density, escaping the low corona near the HCS or a region of low magnetic energy. The CMEs that do not exhibit this behavior ($\delta < 120^\circ$) are analyzed in detailed in Section 3.3. Possible reasons for these events not following the direction of decrease of the magnetic energy can be summarized as: i) if the source region is located close to the HCS and the magnetic forces are large at lower heights, the CME may not necessarily head toward low magnetic-energy regions; ii) if the CME is aimed at a region of open field lines (CH), it is abruptly deflected by the magnetic tension of this structure regardless the local magnetic pressure of the environment. In summary, we find that for these events it is crucial the magnetic forces acting below $2.5\,R_\odot$ and the magnetic tension produced by the CHs, which is not represented in the magnetic-energy-density maps. An additional reason for the discrepancy in the expected behavior of these events may arise from inaccuracies in the deduced locations of the HCS, currently determined from PFSS extrapolations and assuming that the magnetic field is radial above $2.5\,R_\odot$. An apparently important factor related to the amount of total deflection is the speed of the CME relative to the slow solar-wind speed. For CMEs with speeds lower than the slow solar-wind speed (≈ 450 km s^{-1}), the total 3D deflections are larger than for faster CMEs. This is in agreement with previous reports (Gui et al., 2011; Kay, Opher, and Evans, 2015).

The analysis performed here shows that deflections occur both in latitude and longitude. Moreover, the events analyzed exhibit a variety of behaviors, which makes systematization a difficult task. Comprehensive approaches such as the one carried out in the present work for a larger sample of events exhibiting larger deflections, with different characteristics, and observed in different phases of the solar cycle are necessary to gain more insight into the physical mechanisms responsible for the morphological and kinematic properties of their evolution. More realistic models of the magnetic field that take into account its temporal evolution and the different components of magnetic forces are also recommended. This will surely contribute to a broader understanding of the conditions that lead to either a radial or non-radial evolution of a CME event. However, the tracking of prominences and CMEs over several moments of time and in 3D space is a difficult and time-consuming task, which is also affected by the different characteristics and limitations of the instruments used to observe the structures at diverse heights. The PROBA2/SWAP instrument concept of an extended FOV to bridge the gap between other low coronal imagers and coronagraphs is useful in this respect, as it promises to be for its successor onboard PROBA3 (Lamy et al., 2010). In addition, coronagraphs onboard out-of-the-ecliptic missions, such as *Solar Orbiter*'s METIS (Antonucci et al., 2019), will enable better constraining of longitudinal deflections and 3D coordinates of structures overall.

Acknowledgements M.V. Sieyra and M. Cécere acknowledge the PROBA2 Guest Investigator program grant received to carry out this work and the SWAP data provided by the PROBA2 team. M.V. Sieyra acknowledges support from CONICET as postdoc fellow. M. Cécere, H. Cremades, F.A. Iglesias, and A. Costa are members of the Carrera del Investigador Científico (CONICET). A. Sahade is doctoral fellow of CONICET. M. Cécere and A. Sahade acknowledge support from ANPCyT under grant number PICT No. 2016-2480. M. Cécere, M.V. Sieyra, and A. Sahade also acknowledge support by SECYT-UNC grant number PC No. 33620180101147CB. M.V. Sieyra, H. Cremades, and F.A. Iglesias are grateful for the support of project UTN UTI4915TC. M. Mierla, M. West, and E. D'Huys acknowledge support from the Belgian Federal Science Policy Office (BELSPO) through the ESA-PRODEX programme, grant No. 4000120800. G. Stenborg acknowledges the support from the NASA STEREO/SECCHI program NNG17PP27I. The authors are grateful to an anonymous reviewer for useful comments and suggestions. Data courtesy of NASA/SDO and the AIA science team. The SOHO/LASCO data used here are produced by a consortium of the Naval Research Laboratory (USA), Max-Planck-Institut für Aeronomie (Germany), Laboratoire d'Astrophysique de Marseille (France), and the University of Birmingham (UK). SOHO is a mission of international cooperation between ESA and NASA. The STEREO/SECCHI-EUVI, COR1, and COR2 data are produced by an international consortium of the NRL, LMSAL and NASA GSFC (USA), RAL and Univ. Birmingham (UK), MPS (Germany), CSL (Belgium), IOTA and IAS (France). This work utilizes data from the National Solar Observatory Integrated Synoptic Program, which is operated by the Association of Universities for Research in Astronomy, under a cooperative agreement with the National Science Foundation and with additional financial support from the National Oceanic and Atmospheric Administration, the National Aeronautics and Space Administration, and the United States Air Force. The GONG network of instruments is hosted by the Big Bear Solar Observatory, High Altitude Observatory, Learmonth Solar Observatory, Udaipur Solar Observatory, Instituto de Astrofísica de Canarias, and Cerro Tololo Interamerican Observatory.

Disclosure of Potential Conflicts of Interest The authors declare that they have no conflicts of interest.

References

Antonucci, E., Romoli, M., Andretta, V., Fineschi, S., Heinzel, P., Moses, J.D., Naletto, G., Nicolini, G., Spadaro, D., Teriaca, L., Berlicki, A., Capobianco, G., Crescenzio, G., Da Deppo, V., Focardi, M., Frassetto, F., Heerlein, K., Land ini, F., Magli, E., Malvezzi, A.M., Massone, G., Melich, R., Nicolosi, P., Noci, G., Pancrazzi, M., Pelizzo, M.G., Poletto, L., Sasso, C., Schühle, U., Solanki, S.K., Strachan, L., Susino, R., Tondello, G., Uslenghi, M., Woch, J., Abbo, L., Bemporad, A., Casti, M., Dolei, S., Grimani, C., Messerotti, M., Ricci, M., Straus, T., Telloni, D., Zuppella, P., Auchère, F., Bruno, R., Ciaravella, A., Corso, A.J., Alvarez Copano, M., Aznar Cuadrado, R., D'Amicis, R., Enge, R., Gravina, A., Jejčič, S., Lamy, P., Lanzafame, A.r., Meierdierks, T., Papagiannaki, I., Peter, H., Fernandez Rico, G., Giday Sertsu, M., Staub, J., Tsinganos, K., Velli, M., Ventura, R., Verroi, E., Vial, J.-C., Vives, S., Volpicelli, A., Werner, S., Zerr, A., Negri, B., Castronuovo, M., Gabrielli, A., Bertacin, R., Carpentiero, R., Natalucci, S., Marliani, F., Cesa, M., Laget, P., Morea, D., Pieraccini, S., Radaelli, P., Sandri, P., Sarra, P., Cesare, S., Del Forno, F., Massa, E., Montabone, M., Mottini, S., Quattropani, D., Schillaci, T., Boccardo, R., Brando, R., Pandi, A., Baietto, C., Bertone, R., Alvarez-Herrero, A., García Parejo, P., Cebollero, M., Amoruso, M., Centonze, V.: 2019, Metis: the Solar Orbiter visible light and ultraviolet coronal imager. *Astron. Astrophys.* DOI. ADS.

Bemporad, A.: 2009, Stereoscopic reconstruction from STEREO/EUV imagers data of the three-dimensional shape and expansion of an erupting prominence. *Astrophys. J.* **701**, 298. DOI. ADS.

Brueckner, G.E., Howard, R.A., Koomen, M.J., Korendyke, C.M., Michels, D.J., Moses, J.D., Socker, D.G., Dere, K.P., Lamy, P.L., Llebaria, A., Bout, M.V., Schwenn, R., Simnett, G.M., Bedford, D.K., Eyles, C.J.: 1995, The Large Angle Spectroscopic Coronagraph (LASCO). *Solar Phys.* **162**, 357. DOI.

Cécere, M., Sieyra, M.V., Cremades, H., Mierla, M., Sahade, A., Stenborg, G., Costa, A., West, M.J., D'Huys, E.: 2020, Large non-radial propagation of a coronal mass ejection on 2011 January 24. *Adv. Space Res.* **65**, 1654. DOI. ADS.

Cremades, H., Bothmer, V.: 2004, On the three-dimensional configuration of coronal mass ejections. *Astron. Astrophys.* **422**, 307. DOI. ADS.

Cremades, H., Bothmer, V., Tripathi, D.: 2006, Properties of structured coronal mass ejections in solar cycle 23. *Adv. Space Res.* **38**, 461. DOI. ADS.

Cremades, H., Iglesias, F.A., Merenda, L.A.: 2020, Asymmetric expansion of coronal mass ejections in the low corona. *Astron. Astrophys.* **635**, A100. DOI. ADS.

de Koning, C.A., Pizzo, V.J., Biesecker, D.A.: 2009, Geometric localization of CMEs in 3D space using STEREO Beacon data: first results. *Solar Phys.* **256**, 167. DOI. ADS.

Domingo, V., Fleck, B., Poland, A.I.: 1995, The SOHO mission: An overview. *Solar Phys.* **162**, 1. DOI. ADS.

Filippov, B.P., Gopalswamy, N., Lozhechkin, A.V.: 2001, Non-radial motion of eruptive filaments. *Solar Phys.* **203**, 119. DOI. ADS.

Gopalswamy, N., Mäkelä, P., Xie, H., Akiyama, S., Yashiro, S.: 2009, CME interactions with coronal holes and their interplanetary consequences. *J. Geophys. Res. (Space Phys.)* **114**, A00A22. DOI. ADS.

Gosling, J.T., Thomsen, M.F., Bame, S.J., Zwickl, R.D.: 1987, The eastward deflection of fast coronal mass ejecta in interplanetary space. *J. Geophys. Res.* **92**, 12399. DOI. ADS.

Gui, B., Shen, C., Wang, Y., Ye, P., Liu, J., Wang, S., Zhao, X.: 2011, Quantitative analysis of CME deflections in the corona. *Solar Phys.* **271**, 111. DOI. ADS.

Halain, J.-P., Berghmans, D., Seaton, D.B., Nicula, B., De Groof, A., Mierla, M., Mazzoli, A., Defise, J.-M., Rochus, P.: 2013, The SWAP EUV imaging telescope, part II: in-flight performance and calibration. *Solar Phys.* **286**, 67. DOI. ADS.

Howard, R.A., Moses, J.D., Vourlidas, A., Newmark, J.S., Socker, D.G., Plunkett, S.P., Korendyke, C.M., Cook, J.W., Hurley, A., Davila, J.M., et al.: 2008, Sun Earth Connection Coronal and Heliospheric Investigation (SECCHI). *Space Sci. Rev.* **136**, 67. DOI.

Inhester, B.: 2006, Stereoscopy basics for the STEREO mission. arXiv:astro-ph/0612649. ADS.

Isavnin, A., Vourlidas, A., Kilpua, E.K.J.: 2014, Three-dimensional evolution of flux-rope CMEs and its relation to the local orientation of the heliospheric current sheet. *Solar Phys.* **289**, 2141. DOI. ADS.

Kaiser, M.L., Kucera, T.A., Davila, J.M., St. Cyr, O.C., Guhathakurta, M., Christian, E.: 2008, The STEREO mission: an introduction. *Space Sci. Rev.* **136**, 5. DOI.

Kay, C., Gopalswamy, N., Xie, H., Yashiro, S.: 2017, Deflection and rotation of CMEs from active region 11158. *Solar Phys.* **292**, 78. DOI. ADS.

Kay, C., Opher, M., Evans, R.M.: 2015, Global trends of CME deflections based on CME and solar parameters. *Astrophys. J.* **805**, 168. DOI. ADS.

Kennedy, J.R., GONG Team: 1994. Pyper, D.M., Angione, R.J. (eds.) *GONG, a global network of automated solar telescopes*, *ASP CS* **55**, Astron. Soc. Pacific, San Francisco. 188. ADS.

Kilpua, E.K.J., Pomoell, J., Vourlidas, A., Vainio, R., Luhmann, J., Li, Y., Schroeder, P., Galvin, A.B., Simunac, K.: 2009, STEREO observations of interplanetary coronal mass ejections and prominence deflection during solar minimum period. *Ann. Geophys.* **27**, 4491. DOI. ADS.

Lamy, P., Damé, L., Vivès, S., Zhukov, A.: 2010, *ASPIICS: a giant coronagraph for the ESA/PROBA-3 Formation Flying Mission*, *SPIE* **CS-7731**, 773118. DOI. ADS.

Lemen, J.R., Title, A.M., Akin, D.J., Boerner, P.F., Chou, C., Drake, J.F., Duncan, D.W., Edwards, C.G., Friedlaender, F.M., Heyman, G.F., et al.: 2012, The Atmospheric Imaging Assembly (AIA) on the Solar Dynamics Observatory (SDO). *Solar Phys.* **275**, 17. DOI.

Liewer, P.C., de Jong, E.M., Hall, J.R., Howard, R.A., Thompson, W.T., Culhane, J.L., Bone, L., van Driel-Gesztelyi, L.: 2009, Stereoscopic analysis of the 19 may 2007 erupting filament. *Solar Phys.* **256**, 57. DOI. ADS.

Liewer, P.C., Panasenco, O., Hall, J.R.: 2013, Stereoscopic analysis of the 31 August 2007 prominence eruption and coronal mass ejection. *Solar Phys.* **282**, 201. DOI. ADS.

Liewer, P., Panasenco, O., Vourlidas, A., Colaninno, R.: 2015, Observations and analysis of the non-radial propagation of coronal mass ejections near the Sun. *Solar Phys.* **290**, 3343. DOI. ADS.

Liu, Y.D., Luhmann, J.G., Möstl, C., Martinez-Oliveros, J.C., Bale, S.D., Lin, R.P., Harrison, R.A., Temmer, M., Webb, D.F., Odstrcil, D.: 2012, Interactions between coronal mass ejections viewed in coordinated imaging and in situ observations. *Astrophys. J. Lett.* **746**, L15. DOI. ADS.

Liu, Y.D., Luhmann, J.G., Kajdič, P., Kilpua, E.K.J., Lugaz, N., Nitta, N.V., Möstl, C., Lavraud, B., Bale, S.D., Farrugia, C.J., Galvin, A.B.: 2014, Observations of an extreme storm in interplanetary space caused by successive coronal mass ejections. *Nat. Commun.* **5**, 3481. DOI. ADS.

Liu, Y., Thernisien, A., Luhmann, J.G., Vourlidas, A., Davies, J.A., Lin, R.P., Bale, S.D.: 2010, Reconstructing coronal mass ejections with coordinated imaging and in situ observations: global structure, kinematics, and implications for space weather forecasting. *Astrophys. J.* **722**, 1762. DOI. ADS.

Lugaz, N., Farrugia, C.J., Davies, J.A., Möstl, C., Davis, C.J., Roussev, I.I., Temmer, M.: 2012, The deflection of the two interacting coronal mass ejections of 2010 May 23–24 as revealed by combined in situ measurements and heliospheric imaging. *Astrophys. J.* **759**, 68. DOI. ADS.

MacQueen, R.M., Hundhausen, A.J., Conover, C.W.: 1986, The propagation of coronal mass ejection transients. *J. Geophys. Res.* **91**, 31. DOI. ADS.

Maloney, S.A., Gallagher, P.T., McAteer, R.T.J.: 2009, Reconstructing the 3-d trajectories of CMEs in the inner heliosphere. *Solar Phys.* **256**, 149. DOI. ADS.

Martin, S.F.: 2003, Signs of helicity in solar prominences and related features. *Adv. Space Res.* **32**, 1883. DOI. ADS.

Martin, S.F., Panasenco, O., Engvold, O., Lin, Y.: 2008, The link between CMEs, filaments and filament channels. *Ann. Geophys.* **26**, 3061. DOI. ADS.

McCauley, P.I., Su, Y.N., Schanche, N., Evans, K.E., Su, C., McKillop, S., Reeves, K.K.: 2015, Prominence and filament eruptions observed by the solar dynamics observatory: statistical properties, kinematics, and online catalog. *Solar Phys.* **290**, 1703. DOI. ADS.

Mierla, M., Davila, J., Thompson, W., Inhester, B., Srivastava, N., Kramar, M., St. Cyr, O.C., Stenborg, G., Howard, R.A.: 2008, A quick method for estimating the propagation direction of coronal mass ejections using STEREO-COR1 images. *Solar Phys.* **252**, 385. DOI. ADS.

Mierla, M., Inhester, B., Marqué, C., Rodriguez, L., Gissot, S., Zhukov, A.N., Berghmans, D., Davila, J.: 2009, On 3D reconstruction of coronal mass ejections, I: method description and application to SECCHI-COR data. *Solar Phys.* **259**, 123. DOI. ADS.

Mierla, M., Inhester, B., Antunes, A., Boursier, Y., Byrne, J.P., Colaninno, R., Davila, J., de Koning, C.A., Gallagher, P.T., Gissot, S., Howard, R.A., Howard, T.A., Kramar, M., Lamy, P., Liewer, P.C., Maloney, S., Marqué, C., McAteer, R.T.J., Moran, T., Rodriguez, L., Srivastava, N., St. Cyr, O.C., Stenborg, G., Temmer, M., Thernisien, A., Vourlidas, A., West, M.J., Wood, B.E., Zhukov, A.N.: 2010, On the 3-D reconstruction of coronal mass ejections using coronagraph data. *Ann. Geophys.* **28**, 203. DOI. ADS.

Mierla, M., Seaton, D.B., Berghmans, D., Chifu, I., De Groof, A., Inhester, B., Rodriguez, L., Stenborg, G., Zhukov, A.N.: 2013, Study of a prominence eruption using PROBA2/SWAP and STEREO/EUVI data. *Solar Phys.* **286**, 241. DOI. ADS.

Möstl, C., Rollett, T., Frahm, R.A., Liu, Y.D., Long, D.M., Colaninno, R.C., Reiss, M.A., Temmer, M., Farrugia, C.J., Posner, A., Dumbović, M., Janvier, M., Démoulin, P., Boakes, P., Devos, A., Kraaikamp, E., Mays, M.L., Vršnak, B.: 2015, Strong coronal channeling and interplanetary evolution of a solar storm up to Earth and Mars. *Nat. Comm.* **6**, 7135. DOI. ADS.

Müller, D., Nicula, B., Felix, S., Verstringe, F., Bourgoignie, B., Csillaghy, A., Berghmans, D., Jiggens, P., García-Ortiz, J.P., Ireland, J., Zahniy, S., Fleck, B.: 2017, JHelioviewer - time-dependent 3D visualisation of solar and heliospheric data. *Astron. Astrophys.* **606**, A10. DOI. ADS.

Panasenco, O., Martin, S.F.: 2008, In: Howe, R., Komm, R.W., Balasubramaniam, K.S., Petrie, G.J.D. (eds.) *Topological analyses of symmetric eruptive prominences*, *ASP* **CS-383**, Astron. Soc. Pacific, San Francisco, 243. ADS.

Panasenco, O., Martin, S., Joshi, A.D., Srivastava, N.: 2011, Rolling motion in erupting prominences observed by STEREO. *J. Atmos. Solar-Terr. Phys.* **73**, 1129. DOI. ADS.

Panasenco, O., Martin, S.F., Velli, M., Vourlidas, A.: 2013, Origins of rolling, twisting, and non-radial propagation of eruptive solar events. *Solar Phys.* **287**, 391. DOI. ADS.

Pesnell, W.D., Thompson, B.J., Chamberlin, P.C.: 2012, The Solar Dynamics Observatory (SDO). *Solar Phys.* **275**, 3. DOI.

Pevtsov, A.A., Panasenco, O., Martin, S.F.: 2012, Coronal mass ejections from magnetic systems encompassing filament channels without filaments. *Solar Phys.* **277**, 185. DOI. ADS.

Rollett, T., Möstl, C., Temmer, M., Frahm, R.A., Davies, J.A., Veronig, A.M., Vršnak, B., Amerstorfer, U.V., Farrugia, C.J., Žic, T., Zhang, T.L.: 2014, Combined multipoint remote and in situ observations of the asymmetric evolution of a fast solar coronal mass ejection. *Astrophys. J. Lett.* **790**, L6. DOI. ADS.

Santandrea, S., Gantois, K., Strauch, K., Teston, F., Tilmans, E., Baijot, C., Gerrits, D., De Groof, A., Schwehm, G., Zender, J.: 2013, PROBA2: mission and spacecraft overview. *Solar Phys.* **286**, 5. DOI. ADS.

Schrijver, C.J., De Rosa, M.L.: 2003, Photospheric and heliospheric magnetic fields. *Solar Phys.* **212**, 165. DOI. ADS.

Seaton, D.B., Berghmans, D., Nicula, B., Halain, J.-P., De Groof, A., Thibert, T., Bloomfield, D.S., Raftery, C.L., Gallagher, P.T., Auchère, F., Defise, J.-M., D'Huys, E., Lecat, J.-H., Mazy, E., Rochus, P., Rossi, L., Schühle, U., Slemzin, V., Yalim, M.S., Zender, J.: 2013, The SWAP EUV imaging telescope, part I: instrument overview and pre-flight testing. *Solar Phys.* **286**, 43. DOI. ADS.

Seaton, D.B., Mierla, M., Berghmans, D., Zhukov, A.N., Dolla, L.: 2011, SWAP-SECCHI observations of a mass-loading type solar eruption. *Astrophys. J. Lett.* **727**, L10. DOI. ADS.

Shen, C., Wang, Y., Gui, B., Ye, P., Wang, S.: 2011, Kinematic evolution of a slow CME in corona viewed by STEREO-B on 8 October 2007. *Solar Phys.* **269**, 389. DOI. ADS.

Shen, C., Wang, Y., Wang, S., Liu, Y., Liu, R., Vourlidas, A., Miao, B., Ye, P., Liu, J., Zhou, Z.: 2012, Super-elastic collision of large-scale magnetized plasmoids in the heliosphere. *Nature Phys.* **8**, 923. DOI. ADS.

Srivastava, N., Inhester, B., Mierla, M., Podlipnik, B.: 2009, 3D reconstruction of the leading edge of the 20 may 2007 partial halo CME. *Solar Phys.* **259**, 213. DOI. ADS.

Temmer, M., Preiss, S., Veronig, A.M.: 2009, CME projection effects studied with STEREO/COR and SOHO/LASCO. *Solar Phys.* **256**, 183. DOI. ADS.

Thernisien, A., Vourlidas, A., Howard, R.A.: 2009, Forward modeling of coronal mass ejections using STEREO/SECCHI data. *Solar Phys.* **256**, 111. DOI. ADS.

Thernisien, A., Vourlidas, A., Howard, R.A.: 2011, CME reconstruction: pre-STEREO and STEREO era. *J. Atmos. Solar-Terr. Phys.* **73**, 1156. DOI. ADS.

Thernisien, A.F.R., Howard, R.A., Vourlidas, A.: 2006, Modeling of flux rope coronal mass ejections. *Astrophys. J.* **652**, 763. DOI. ADS.

Vandas, M., Fischer, S., Dryer, M., Smith, Z., Detman, T.: 1996, Simulation of magnetic cloud propagation in the inner heliosphere in two dimensions, 2: a loop parallel to the ecliptic plane and the role of helicity. *J. Geophys. Res.* **101**, 2505. DOI. ADS.

Wang, R., Liu, Y.D., Dai, X., Yang, Z., Huang, C., Hu, H.: 2015, The role of active region coronal magnetic field in determining coronal mass ejection propagation direction. *Astrophys. J.* **814**, 80. DOI. ADS.

Wang, Y., Chen, C., Gui, B., Shen, C., Ye, P., Wang, S.: 2011, Statistical study of coronal mass ejection source locations: understanding CMEs viewed in coronagraphs. *J. Geophys. Res. (Space Phys.)* **116**, A04104. DOI. ADS.

Xie, H., St. Cyr, O.C., Gopalswamy, N., Yashiro, S., Krall, J., Kramar, M., Davila, J.: 2009, On the origin, 3D structure and dynamic evolution of CMEs near solar minimum. *Solar Phys.* **259**, 143. DOI. ADS.

Yashiro, S., Gopalswamy, N., Michalek, G., St. Cyr, O.C., Plunkett, S.P., Rich, N.B., Howard, R.A.: 2004, A catalog of white light coronal mass ejections observed by the SOHO spacecraft. *J. Geophys. Res. (Space Phys.)* **109**, A07105. DOI. ADS.

Zhuang, B., Wang, Y., Shen, C., Liu, S., Wang, J., Pan, Z., Li, H., Liu, R.: 2017, The significance of the influence of the CME deflection in interplanetary space on the CME arrival at Earth. *Astrophys. J.* **845**, 117. DOI. ADS.

Zhuang, B., Wang, Y., Hu, Y., Shen, C., Liu, R., Gou, T., Zhang, Q., Li, X.: 2019, Numerical simulations on the deflection of coronal mass ejections in the interplanetary space. *Astrophys. J.* **876**, 73. DOI. ADS.